

EarthArXiv pre-print – this manuscript is not peer-reviewed

1 **Foraminiferal Analysis of Holocene Sea Level Rise within Trinity**

2 **River Incised Paleo-Valley, Offshore Galveston Bay, Texas**

3 Standring, P.^{1,2*}, Lowery, C.¹, Burstein, J.^{1,2,^}, Swartz, J.^{1,2,#}, Goff, J.^{1,2}, Gulick, S.P.S.^{1,2}

4 ¹Institute for Geophysics, University of Texas at Austin, Texas

5 ²Department of Geological Sciences, University of Texas at Austin, Austin, Texas

6 *Corresponding Author: patty.standring@utexas.edu

7 #Now at: Water Institute of the Gulf, Baton Rouge, Louisiana

8 ^Now at: T. Baker Smith, LLC, Aransas Pass, Texas

9

10

11

12 This manuscript is a non-peer reviewed EarthArXiv pre-print. It has
13 been submitted for publication in Marine Geology.

14

15

16

17

18

19

20

21

22

23

24 **Highlights:**

- 25 • Micropaleontology as environmental context for seismic and sedimentologic analysis
- 26 • Long-term (~2 kyr) stable estuary amid early Holocene sea-level rise
- 27 • Revised paleoshoreline model matching characteristic geometry of modern shoreline

28 **Abstract**

29 Sea-level is expected to continue to rise in the next century, and as society prepares to deal with
30 this hazard it is critically important to understand how coastal systems will respond, especially in
31 regions with rapid rates of coastal erosion and relative sea-level rise like the Gulf of Mexico
32 Texas coast. Tide gauge records in Galveston Bay, Texas, indicate that local sea level rise rates
33 are more than twice the global average, raising important questions about the long-term stability
34 of the barrier islands protecting the bay and how the estuary and coastline will respond to sea-
35 level rise. However, tide gauge records only go back to the beginning of the last century, and
36 longer records are needed to provide insight into dynamic coastal response to sea-level
37 fluctuations. Here, we combine geophysical (chirp sub-bottom profiler) surveys and sediment
38 cores (providing sedimentological and micropaleontological data constrained by radiocarbon
39 dating) to characterize paleoenvironmental change in the Holocene estuary system offshore
40 modern Galveston Bay over the last ~10 kyr; with the first 4 kyr of this time span undergoing a
41 period of rapid sea level rise more than twice the modern rate. Our foraminiferal analysis
42 provides ecological context on the stability of these paleoenvironments and the timing of coastal
43 change over the last ~10 kyr. We provide a model of Holocene shoreline change differing from
44 existing interpretations of rapid landward shifts with asymmetric coastal geometry to one
45 composed of more gradual transitions matching modern coastal geometry and argue for an
46 overall stable paleoestuarine environment throughout the middle Holocene (~6.9 ka – 8.8 ka).

47 Subsequent shoreline shifts occurred after global sea level rise slowed below modern rates,
48 indicating hydroclimate impacts on sediment flux likely had a greater influence on the earlier
49 stability of the estuarine system and later shoreline retreat than rates of sea-level rise.

50

51 Keywords: Sea level change, micropaleontology (forams), N America

52

53 **1. Introduction**

54 As global sea levels continue to rise, constraining how coastlines respond is increasingly
55 important for coastal planning. High estimates of sea-level rise exceed 2 m above current mean
56 levels by 2100 for +5°C of warming, in which CO₂ emissions are not curbed, while lower
57 estimates for +2°C of warming, which falls in line with plans that cut CO₂ emissions globally,
58 put sea-level rise at 0.26-0.81 m by 2100 (Bamber et al., 2019). Although the most recent
59 Intergovernmental Panel on Climate Change Assessment Report indicates low confidence for
60 higher end estimates of sea-level rise by 2100, these estimates “cannot be ruled out due to the
61 deep uncertainty in ice processes” (IPCC, 2021). Even this lower range of sea level rise presents
62 a significant threat to coastal communities (Bamber et al., 2019; Bernstein et al., 2019) which
63 represent ~10% of the world’s population (FitzGerald et al., 2008). A 1.8 m rise in sea level
64 would inundate six million coastal homes in the U.S. and risks one trillion dollars in damage to
65 coastal residential real estate (Bernstein et al., 2019). Global mean sea-level rise does not impact
66 areas equally and some areas will experience significantly higher flooding rates over the next
67 century (Vitousek et al., 2017); thus, it is important to understand regional and local coastal
68 response to rising seas.

69

EarthArXiv pre-print – this manuscript is not peer-reviewed

70 Low-gradient, low-elevation coastlines around the Gulf of Mexico are especially vulnerable to
71 the destruction caused by large storms and hurricanes, requiring significant periods of time for
72 barrier island systems to adjust and recover (Bernstein et al., 2019; FitzGerald et al., 2008; Goff
73 et al., 2010; Palermo et al., 2021; Shawler et al., 2021). Industrial development, dredging for
74 navigation purposes in the back-barrier, reduction of natural wetlands, and increased subsidence
75 due to extraction of hydrocarbons and groundwater contribute to the Gulf Coast's vulnerability
76 to sea level rise and coastal inundation, particularly in areas like Galveston Bay (Anderson et al.,
77 2008; Kirwan and Megonigal, 2013; Paine, 1993; Shawler et al., 2021; White et al., 2002).

78 Despite recent local regulations concerning groundwater extractions, compaction and subsidence
79 from 20th century pumping is estimated to continue over several hundred years (Miller and
80 Shirzaei, 2021). As the busiest shipping center in the U.S. (Port of Houston, 2021), Galveston
81 Bay represents a particular vulnerability of U.S. supply chains and infrastructure due to sea level
82 inundation. As a result of heavy development, the western boundary of Galveston Bay no longer
83 consists of protective wetlands (Anderson et al., 2008) and overall wetland loss in the Trinity
84 River delta area exists due to subsidence and relative sea level rise (White et al., 2002). Barrier
85 islands, like those that enclose Galveston Bay, evolve due to sea-level rise on centennial to
86 millennial timescales, and sediment transport along the shoreline, with local-scale conditions
87 altering the timing of barrier erosion and progradation processes (Fruergaard et al., 2015; Lentz
88 et al., 2013; Raff et al., 2018; Shawler et al., 2021). These processes are also highly influenced
89 by antecedent topography and slope, and sediment supply within the substrate, where muddier
90 substrates result in barriers that are prone to collapse and drowning, and shallower slopes will
91 experience more rapid drowning and disintegration of barrier systems than steeper slopes under
92 the same rate of sea-level rise (Brenner et al., 2015; Lorenzo-Trueba and Ashton, 2014; Moore et

93 al., 2010; Raff et al., 2018; Shawler et al., 2021). In general, shallower back-barrier
94 environments experience more rapid landward migration of barrier islands (Lorenzo-Trueba and
95 Ashton, 2014; Moore et al., 2010; Shawler et al., 2021). As back-barrier marshes and coastal
96 wetlands are inundated and converted to intertidal and subtidal environments, the tidal prism of
97 the bay is enlarged, which increases the volume of sand contributed to ebb- and flood-tidal deltas
98 (Al Mukaimi et al., 2018; FitzGerald et al., 2008). This process leads to the denudation of barrier
99 systems, furthering the erosion of coastal environments (FitzGerald et al., 2008).

100

101 Understanding how specific areas of the Gulf Coast have responded to relative sea level rise in
102 the past provides predictions for future coastal vulnerabilities, especially in populated areas that
103 are undergoing rapid coastal land loss, like Galveston Bay, Texas (Anderson et al., 2016, 2008;
104 Phillips et al., 2004; White et al., 2002). Flood hazard assessments predict over 76 km² along the
105 Texas coast will subside below sea level by 2100, which alone increases the area of inundation
106 due to sea-level rise by 39% (Miller and Shirzaei, 2021). Subsidence within Galveston Bay is
107 lowest near the mouth of the San Jacinto River and the Houston Ship Channel, and although
108 sedimentation rates are higher in this area than the rest of Galveston Bay, they are almost 50%
109 lower than rates of sea-level rise generating an accretionary deficit (Al Mukaimi et al., 2018).

110

111 Instrumental records help identify trends in sea level changes along the coasts, while highlighting
112 specific coastal regions at increased risk of land loss. Monthly mean sea level measurements at
113 Galveston Bay Pier 21 establish relative sea-level rise trends with a 95% confidence level of
114 $+6.59 \pm 0.22$ mm yr⁻¹ over the time period from 1904-2020, and at $+6.62 \pm 0.69$ mm yr⁻¹ from
115 1957-2011 for Galveston Pleasure Pier (NOAA, 2021). This rate is significantly higher than all

116 other stations along the Texas Coast, and even double in some cases. For example, Padre Island
117 data show a sea-level rising trend of $+3.48 \pm 0.75$ mm yr⁻¹ from 1958-2006, and $+3.54 \pm 0.70$
118 mm yr⁻¹ at Port Mansfield, Texas, from 1963-2020 (NOAA, 2021). Nearby Sabine Pass, Texas,
119 shows a similar, but lower, trend of $+6.16 \pm 0.74$ mm yr⁻¹ from 1958-2020 (NOAA, 2021).
120 Observations of coastal erosion by the Texas Bureau of Economic Geology show a net retreat of
121 1.24 m yr⁻¹ for the entire Texas coast, and a rate of 0.4 m yr⁻¹ for Galveston County on the
122 western side of Galveston Bay, and 1.63 m yr⁻¹ for Chambers County on the eastern side of
123 Galveston Bay (Paine et al., 2011). The report specifically highlighted the area of sandy beach
124 west of the seawall on Galveston Island as undergoing significant shoreline retreat, whereas
125 longshore current causes net shoreline advance on Bolivar Peninsula east of the Bolivar Roads
126 tidal inlet, which is likely due to the construction of jetties on either side of the inlet (Paine et al.,
127 2011).

128
129 Unfortunately, instrumental data are limited by the short timescales they cover, on the Gulf Coast
130 only going as far back as the early 1900s (and more commonly several decades later). These
131 instrument records often start after accelerated sea-level rise has been initiated, introducing a
132 potential bias in future rising sea level predictions and modeling (Horton et al., 2019). Therefore,
133 it is necessary to use the geologic record to augment the instrumental data and determine how
134 past coastal changes have been influenced by accelerated sea level rise (Horton et al., 2019).

135
136 Looking further back in time provides insight into the impact of rapid sea level rise on coastlines
137 (Dutton et al., 2015; Horton et al., 2019). As part of a Bureau of Ocean Energy Management
138 funded effort to identify subsurface sand resources along the Gulf shelf for coastal resilience and

139 nourishment projects, the Trinity River Incised Paleo-Valley Project has conducted multiple
140 seismic surveys and sediment coring to map the Trinity River-incised valley offshore modern
141 Galveston Bay and chart its transformation from a Pleistocene fluvial to Holocene estuarine to
142 modern open marine environment. Here, we use high-resolution seismic data in combination
143 with micropaleontological analysis, sedimentology, carbon dating, and age modeling from
144 sediment cores to develop a comprehensive history of Holocene paleoenvironmental and coastal
145 change in the Trinity paleo-valley over the last 10 kyr, during which time sea level rise slowed
146 from 5 mm yr⁻¹ to 3 mm yr⁻¹ (Milliken et al., 2008). We identify periods of estuary stability
147 through barrier island development and subsequent shoreline retreat.

148

149 **2. Regional Setting/Background**

150 Modern Galveston Bay is located on the northeast Texas coast in the Gulf of Mexico and
151 consists of multiple bays that comprise the Estuary Complex (Figure 1). The microtidal, wave-
152 dominated regime in the Gulf of Mexico allows for long, narrow, relatively straight barrier island
153 system protecting the estuary, consisting of Bolivar Peninsula on the eastern side of the bay and
154 Galveston Island on the western side (Anderson et al., 2016, 2014; Davis and Hayes, 1984;
155 FitzGerald et al., 2008; Rodriguez et al., 2004). The shape of Galveston Bay developed when
156 existing fluvial topography was inundated as the bay mouth was restricted to a tidal inlet ~2.5 ka
157 (Anderson et al., 2016, 2008; Rodriguez et al., 2004). Construction of jetties has restricted
158 sediment flow through Bolivar Roads, the primary inlet into the estuary (Anderson et al., 2008;
159 Siringan and Anderson, 1993).

160

EarthArXiv pre-print – this manuscript is not peer-reviewed

161 John Anderson and his research group at Rice University established a firm foundation of
162 research on modern Galveston Bay and its transformation throughout the Holocene (Anderson et
163 al., 2016, 2014, 2008; Milliken et al., 2008; Rodriguez et al., 2005, 2004; Simms et al., 2007;
164 Siringan and Anderson, 1993). During Marine Isotope Stages (MIS) 5-3, the region experienced
165 episodic sea-level fall, which led to the creation of Trinity and San Jacinto incised river valley
166 (Figure 2 & 3) (Anderson et al., 2016, 2014; Swartz, 2019). Stepped downcutting throughout the
167 incised valley resulted in terraced morphology (Anderson et al., 2016, 2008; Rodriguez et al.,
168 2005). The upper, wider portions of the incised valley are not visible in the sediment record
169 because they have been removed by shoreface erosion to the transgressive ravinement during
170 Holocene sea-level rise, identified at -8 to -10 m depth along the Texas coast as the onlapping of
171 marine muds onto a “decapitated shoreface” (Anderson et al., 2016; Rodriguez et al., 2004).
172
173 Global sea-level rise between ~11.4 and 8.2 ka is estimated at ~15 m kyr⁻¹ followed by a reduced
174 rate of sea-level rise 8.2-6.7 ka, coinciding with the final deglaciation of North America
175 (Lambeck et al., 2014). Along the Gulf Coast, sea level began to rise episodically between ~10
176 and 7 ka, after which it slowed to steady present day levels (Figure 2) (Anderson et al., 2016,
177 2014; Milliken et al., 2008; Swartz, 2019). The Anderson group identified multiple flooding
178 surfaces within the Trinity incised valley that occur either contemporaneously with other areas
179 along the Gulf coast and are attributed to rapid sea-level rise, or exist locally, suggesting forcing
180 mechanisms such as changing sediment supply and/or antecedent topography (Anderson et al.,
181 2016; Rodriguez et al., 2005). Radiocarbon dating in sediment cores from modern Galveston Bay
182 constrain rapid sea-level rise events to 9.6 ka, 8.2 ka, and between 7.7 and 7.4 ka, in which each
183 inundation was complete after only a few centuries (Figure 4) (Anderson et al., 2008). Milliken

184 et al., (2008) identified flooding events consistent with radiocarbon dates and relative sea level
185 changes within the Gulf of Mexico at 9.5-9.8 ka, 8.5-8.9 ka, 8.0-8.4 ka, and 6.8-7.4 ka (Figure
186 2).

187
188 Estimates of Antarctic ice-sheet fluctuations since the Last Glacial Maximum vary widely, so
189 most Holocene sea-level rise is attributed to the better constrained demise of the Laurentide Ice
190 Sheet (LIS), with some evidence for Antarctic melting after ~6 ka (Lambeck et al., 2014). Higher
191 resolution analysis of LIS deglaciation reveals multiple meltwater pulses at 9.1 ka, 8.7 ka, 8.6 ka,
192 and 8.2 ka, and 7.4 ka (Jennings et al., 2015). After 8.15 ka, LIS retreat accelerated with remnant
193 ice domes melting by ~6.7 ka (Lambeck et al., 2014; Ullman et al., 2016). Remaining global sea-
194 level rise is attributed to the loss of ice volume from the West Antarctic ice-sheet during the late
195 Holocene (Ullman et al., 2016).

196
197 Approximately 9.6 ka, the initial inundation of modern Galveston Bay shifted the upper bay ~30
198 km up the incised valley, coincident with LIS retreat and Hudson Strait freshwater drainage
199 (Anderson et al., 2008; Jennings et al., 2015; Lambeck et al., 2014; Thomas and Anderson,
200 1994). The early opening of the Tyrell Sea ~8.6 ka and the catastrophic release of freshwater
201 from North American glacial lakes occurred at 8.15 ka (Jennings et al., 2015). At the same time
202 the bayhead delta shifted ~10 km up the valley, partially attributed to a “dramatic decrease in
203 sedimentation rates” from 4.6 mm yr⁻¹ to 1.3 mm yr⁻¹ and the coincident elevation of a
204 Pleistocene-age terrace (Figure 4) (Anderson et al., 2008). Higher temperatures in the Atlantic
205 Meridional Overturning Circulation, likely due to Antarctic ice sheet loss, and strengthening of
206 the North Atlantic Deep Water led to a warming period 7.9 ka (Cronin et al., 2007) in which

207 remnant ice domes of the LIS were significantly melted (Ullman et al., 2016). Between 7.7 and
208 7.4 ka the upper bay shifted a further ~25 km up the valley at a rate of 8 km century⁻¹ but
209 maintained its existing shoreline ~50 km seaward of the modern coastline, which produced a
210 ~100-km-long paleoestuary (Anderson et al., 2008; Rodriguez et al., 2005). This flooding event
211 occurred despite the decreasing rate of sea-level rise between 7.5 and 7.0 ka, with coincident
212 events in Matagorda Bay and Sabine Lake, and is attributed to a Gulf Coast climate transition
213 from cool and moist to warm and dry, reducing sediment supply (Anderson et al., 2008).

214

215 Radiocarbon dating of sandy sediments from Heald Bank suggest that the paleoshoreline was in
216 that location by as late as 7.7 ka, while ages obtained from the oldest beach ridges on Galveston
217 Island constrain its development to 5.5 ka (Figure 1) (Anderson et al., 2014, 2008; Rodriguez et
218 al., 2005, 2004). Conflicting interpretations of Heald Bank sands call into question the 7.7-ka-
219 shoreline, and suggest the bank may be marine in origin, like Thomas and Shepard Banks, and
220 developed after the shoreline had already shifted up-valley (Thomas and Anderson, 1994).

221 Bolivar Peninsula began to develop as a spit ~2.5 ka and as it prograded westward, the tidal inlet
222 narrowed to a fraction of its original size to form Bolivar Roads tidal inlet allowing flooding
223 along the bay boundaries, establishing the modern shape of Galveston Bay (Anderson et al.,
224 2016, 2014, 2008; Rodriguez et al., 2005, 2004).

225

226 Although prior sedimentological and seismic research conducted by the Anderson group is
227 thorough, it has thus far lacked sufficient paleoenvironmental evidence and the spatial coverage
228 necessary to establish the evolution of the paleo-estuary (Anderson et al., 2008; Rodriguez et al.,
229 2004). Additional higher resolution seismic data combined with radiocarbon dating of sediment

230 cores and micropaleontological interpretations of facies changes will characterize coastal change
231 by temporally and spatially constraining a large and long-term stable estuarine environment and
232 the transformation of the coastline throughout the Holocene. Foraminifera are powerful proxies
233 for paleoenvironmental and relative sea level change because of their sensitivity to temperature,
234 salinity, and nutrient availability (Culver, 1988; Gehrels, 2013; Olson and Leckie, 2003; Phleger,
235 1951; Poag, 1981). Modern assemblages represent a specific “physicochemical environment”
236 within ecological niches or biozones that can be translated to fossil assemblages in sediment
237 cores to identify paleoenvironmental changes as a result of relative sea level fluctuations forming
238 a link between instrumental and fossil records (Culver, 1988; Phleger, 1960; Gehrels, 2013;
239 Olson and Leckie, 2003; Phleger, 1965; Poag, 1981). This link allows us to differentiate upper,
240 middle, and outer bay environments within otherwise unremarkable successions of estuarine mud
241 and separate sandy ebb- and flood-tidal delta deposits from back-barrier washover fans. Benthic
242 foraminiferal assemblages provide paleoenvironmental context to seismic data and allow for the
243 clarification of the timing of the inundation of the Trinity River Paleovalley and the
244 interpretation of barrier island stability and rollover rate amid rising sea levels at a higher
245 resolution than has previously been possible.

246

247 **3. Methods**

248 *3.1 Seismic Data*

249 Approximately 1,000 km of high-resolution seismic data were obtained during two field courses
250 and two cruises funded by the Bureau of Ocean and Energy Management (BOEM) for the
251 purpose of researching sand deposits. These surveys were conducted with an EdgeTech 512i sub-
252 bottom profiler with 0.7 to 12 kHz frequency sweep, 20 ms pulses by the University of Texas

253 Institute for Geophysics (UTIG) (Figure 1). These data were incorporated with 690 line-km of
254 high-resolution chirp seismic surveys conducted by Texas A&M Galveston and the U.S.
255 Geological Survey (USGS) in 2009 using EdgeTech Geo-Star FSSB system and SB-0512i
256 towfish with 20 ms pulse length and 0.7-12 kHz sweep frequency aboard the R/V Manta
257 (Dellapenna et al., 2009). Processing of UTIG chirp data and interpretation of seismic horizons
258 were conducted by Swartz (2019) and Burstein et al., 2021. UTIG data include full-waveform
259 processing providing a higher resolution of the subsurface stratigraphy (Goff et al., 2015).
260 Seismic lines corresponding to sediment cores were converted from two-way travel time in
261 milliseconds to meters with an approximate seismic wave velocity of 1525 m s^{-1} (Abdulah et al.,
262 2004).

263

264 *3.2 Piston and gravity coring*

265 Piston core (PC) sites (Figure 1) were chosen based on sedimentary structures observed in
266 seismic data to pinpoint key transitions in the sedimentary record and evaluate
267 paleoenvironmental evolution from fluvial to estuarine to modern-day marine. Piston cores were
268 collected during a cruise of the R/V *Brooks McCall* as part of UTIG's 2018 Marine Geology and
269 Geophysics (MGG) Field Course. Gravity core (GC) locations (Figure 1) were selected during
270 processing to clarify additional points of interest, particularly along the valley edges, and were
271 collected during a BOEM-UTIG cruise of the R/V *Manta* in 2019.

272

273 Piston and gravity cores were split onshore after both cruises were completed. The archive
274 halves were stored, and the working halves were described for appearance, visual grain size,
275 bioturbation, and presence of marine fauna (e.g., shell fragments and shell hash), and terrestrial

276 organic material (e.g., plant debris). Sediment samples for microfossil analysis were selected at
277 10- to 50-cm intervals from piston and gravity cores, and at specific points where a
278 paleoenvironmental transition may have occurred based on changes observed in the core,
279 avoiding sandier sediments. Piston core 2 (PC-2) was the longest core collected and was sampled
280 at higher resolution to serve as a reference section. Subsequent sampling in piston core 4 (PC-4)
281 and all the gravity cores (GC-1 thru GC-6) was done at a lower resolution with additional
282 samples selected to more precisely identify paleoenvironmental transitions. Samples were soaked
283 for at least 24 hours in a mixture of borax and hydrogen peroxide to break down clay floccules,
284 washed over a 63- μ m sieve, and dried in an oven.

285

286 3.3 Foraminiferal analysis

287 Samples were split to provide a reasonable amount of material and foraminifera were picked
288 using a binocular microscope and placed on a slide. Population sizes of at least 100 foraminifera
289 tests were picked where possible (some samples were barren or did not yield 100 individuals)
290 and identified at the genus level. Foraminifera that were not identifiable at the genus level were
291 classified as “benthic spp.” Confidence interval calculations (see Appendix A) show that these
292 population sizes are sufficient to track changes in predominance facies (i.e., *Ammonia* vs.
293 *Elphidium*) within the estuary. Confidence intervals were based on the binomial method
294 provided in Buzas (1990). Modern grab samples from Bolivar Roads tidal inlet obtained during
295 the MGG 2018 Field Course were analyzed and used as a comparison for flood- and ebb-tidal
296 delta sediments in the cores. Samples were soaked overnight in a 1% solution of Rose Bengal
297 and water immediately after collection to stain specimens which were living or recently living.

298 Samples were then sieved and dried in an oven. Populations of at least 300 individuals were
299 picked and identified at the genus level (see Appendix A).

300

301 Predominance facies are defined by genus of foraminifera (Culver, 1988; Poag, 1981). Poag
302 (1981) synthesized analysis of modern benthic foraminiferal assemblages in the Gulf of Mexico
303 (Figure 5) and outlined predominance facies for Galveston Estuary Complex based on the
304 previous work conducted by Wantland (1969) within the Trinity Bay and written communication
305 from W.V. Sliter of the USGS. Wantland (1969) collected 87 samples from stations within the
306 subaerial Trinity River delta and Trinity Bay and used Rose Bengal solution to determine live
307 taxa at time of collection. Live samples were picked from 62- μ m sieved wet sediments and
308 populations were based on at least 300 individual tests where possible (Wantland, 1969). Poag
309 (1981) identified the following modern predominance facies for Galveston Bay: dominance of
310 *Ammotium* represented upper bay or river delta facies, dominance of *Ammonia* indicated central
311 bay facies, and dominance of *Elphidium* was determined to be outer bay facies (Figure 5). Culver
312 (1988) also outlined a priori groups of prominent foraminifera genera by depth and
313 environmental preference, which match well with Poag's predominance facies. Culver (1988)
314 specified genera of foraminifera that can be considered diagnostic of certain environments:
315 *Ammotium* for marshes, *Ammobaculites* and *Elphidium* for bays/estuaries, and *Bolivina* spp.,
316 *Bulimina* spp., and *Elphidium* spp. for inner shelf environments (Figure 5).

317

318 Paleoenvironmental interpretations of the Holocene estuary system are based off of assemblage
319 percentages of three primary genera outlined by Poag (1981). Samples with >50% *Ammonia* are
320 interpreted as central bay facies, samples with ~50-50 *Ammonia/Elphidium* are transitional to

321 outer bay, and samples with >50% *Elphidium* are outer bay facies. *Ammotium*, indicative of
322 Poag's bayhead delta facies, was typically not identifiable at the genus or species level due to
323 test fragmentation. Agglutinated taxa are generally uncommon and are poorly preserved in our
324 cores, so they were categorized as agglutinated spp. We interpret increases in the presence of
325 agglutinated spp. to indicate proximity to bay margin environments that are more likely to be
326 dominated by agglutinated taxa. An overall increase in diversity including common inner shelf
327 taxa (e.g., *Bulimina*, *Bolivina*, miliolids, etc.) coupled with a resurgence of *Ammonia* spp. likely
328 indicates a transition to modern marine or open shelf facies (Culver, 1988; Olson and Leckie,
329 2003; Poag, 1981). Facies lacking in foraminifera were deemed barren and, given their
330 stratigraphic position, interpreted to reflect the transition to terrestrial (e.g., fluvial)
331 environments.

332
333 Estuaries are dynamic environments and reworking of material is likely common. To identify
334 areas of potential reworking, foraminiferal test fragments (interpreted to be broken during
335 redeposition) within each sample were counted in addition to individual identifiable tests for
336 population totals. Total fragments were normalized to total foraminifera to provide a percent
337 fragmentation for each sample. Peaks in fragmentation are interpreted as potential periods of
338 increased energy or sediment reworking, and in some cases coincided with decreased foram
339 populations.

340

341 3.4 Radiocarbon dating

342 Sediment cores were sampled for radiocarbon dating to provide age constraints on
343 paleoenvironmental transitions and develop age models for each core. A total of 28 samples were

344 sent to the National Ocean Sciences Accelerator Mass Spectrometry (NOSAMS) at Woods Hole
345 Oceanographic Institute for radiocarbon dating using the Libby half-life of 5,568 yr and
346 corrected for carbon isotopic fractionation. Of these samples, 23 were mollusk shells, 2 were
347 comprised of foraminiferal tests, and 3 contained organic material/plant debris (Table 1).
348 Mollusk and foraminiferal samples containing at least 4 mg of material underwent hydrolysis
349 where carbon in the samples were converted to CO₂ using a strong acid H₂PO₃. Mollusk samples
350 were powdered to allow NOSAMS staff to subsample material >9 mg. Radiocarbon dates from
351 organic material were calibrated with IntCal20 (Reimer et al., 2020) and mollusk and
352 foraminifera ages were corrected for reservoir variations using a correction specific to the Gulf
353 of Mexico offshore Galveston Bay (Wagner et al., 2009) and then calibrated using Marine20
354 (Heaton et al., 2020). The IntCal20 calibrations were done via OxCal 4.4 (Ramsey, 2009) and the
355 Marine20 calibrations were applied through Bchron (Haslett and Parnell, 2008). Errors in ages
356 were calculated by NOSAMS where the error is determined by the larger of two estimates, the
357 internal statistical error calculated using the total number of ¹⁴C counts (error = 1/√n) and the
358 external error determined by the ratio of ¹⁴C and ¹²C of a sample calculated 10 separate times
359 while the sample was being run.

360

361 *3.5 Age models*

362 Age models were developed using the code rbacon (Blaauw and Christen, 2011), which
363 calculates sediment accumulation rates based on a gamma autoregressive semiparametric model
364 using a Markov chain Monte Carlo algorithm. The model provides a predictive window with
365 95% confidence of the age of sediments given depth and radiocarbon age constraints and the
366 assumption of consistent deposition unless hiatuses are applied. Although we suspect a

367 significant amount of erosion may have occurred during transgression, the lack of upper core
368 carbon dates limits the application of hiatus depths in the model and interpolated ages for the
369 upper core are likely incorrect. Interpolated ages from the models for each core (except for GC-
370 1) were used to identify environmental transitions between radiocarbon ages, and in a few
371 instances, extrapolated ages were used to identify transitions outside the range of carbon dates.

372

373 **4. Results**

374 Sediment cores range from <1 m to ~ 5.6 m in depth and primarily contain medium-gray mud
375 varying from clay to silty-clay with sandy intervals that occasionally coincide with shell hash
376 layers or abundant shell fragments (Figure 6). GC-4 contains significantly more organic material
377 and less shell material than all the other cores. GC-1 and PC-4 contain sharp and gradual
378 contacts, respectively, between stiff, light-gray Pleistocene clay terraces and Holocene sediments
379 (Figure 6h & 6b). PC-2 and PC-4 did not contain any analyzable upper seafloor sediments due to
380 coring disturbance caused by over-penetration of the piston corer and the soupy nature of the
381 uppermost sediments. Here, we summarize the key observations for each core, proceeding from
382 the most proximal to most distal core.

383

384 *4.1 Piston core 2*

385 PC-2 was selected for identification of a fluvial terrace toward the western edge of the incised
386 valley (Figure 7A). It consists primarily of massive medium-gray clay with sporadic sandy layers
387 that coincide with increased shell fragments and in some cases shell hash layers (Figure 7). The
388 core catcher contains silty medium sand which is overlain by silt and clay (Figure 6a). As the
389 reference section representing the complete transition from fluvial to outer bay deposition, this

390 core was sampled at the highest resolution at least every 10 cm. The base of the core is barren of
391 foraminifera and is interpreted as fluvial deposits, which are capped by upper bay/deltaic
392 deposits dominated by agglutinated benthics and dated to $9,794 \pm 215$ cal yr B.P. from a mollusk
393 shell at 5.10 m depth (Figure 7B). The increase in percentage of fragmented foraminifera tests
394 represents a higher energy environment with potentially more reworked material (Figure 7B).
395 Upper bay deposits transition at ~ 9.5 ka upward into ~ 2.8 m of central bay sediments that are
396 generally dominated by *Ammonia* with some increases in presence of *Elphidium*. The age model
397 of this core (Figure 7B) indicates that this central estuary assemblage existed from at least 9.5 to
398 8.0 ka, indicating a long period of stability in the estuary system during this time. By $7,800 \pm 134$
399 cal yr B.P. (mollusk shell at 1.82 m), the environment had transitioned to outer bay, with a
400 foraminiferal assemblage dominated by *Elphidium*. The uppermost meter of the core was not
401 analyzed due to coring disturbance.

402

403 4.2 Piston core 4

404 PC-4 was obtained at the location of another fluvial terrace originally interpreted seismically to
405 be a point bar (Figure 8A), but which was instead revealed to be a Pleistocene flood plain deposit
406 comprised of light-gray, stiff Beaumont Clay, into which the MIS5-3 river valley was incised.
407 The terrace is heavily laminated with oxidized sand layers and contains a calcareous nodule,
408 which are relatively common in the Beaumont (Rehkemper, 1969). The terrace gradually
409 transitions upward into heavily burrowed sand (Figure 6b), and both the terrace and the
410 overlying sandy section are barren of microfossils and interpreted as fluvial/terrestrial sediments.
411 At approximately 3.5 m depth, foraminiferal assemblages appear in the sandy sediments and
412 indicate a transition to an upper bay environment, dated to $9,131 \pm 158$ cal yr B.P. (mollusk shell

413 at 3.44 m) (Figure 8B). These sediments also contain visible burrows and a higher percentage of
414 fragmented foraminifera tests. PC-4 contains less central bay sediments compared to PC-2, likely
415 due to the elevation of the Pleistocene terrace. The seismic data show draping of sediments
416 above and over the terrace (Figure 8A). Central bay sediments were dominated by *Ammonia* and
417 dated to $8,815 \pm 175$ cal yr B.P. by a mollusk shell at 2.66 m depth. At approximately 2 m depth,
418 *Elphidium* becomes more dominant and the environment transitions to outer bay sediments.
419 According to the age model for this core (Figure 8B), the central bay to outer bay transition
420 occurred ~ 8.0 ka, coinciding with the same transition in PC-2. The increase in diversity of
421 foraminifera at ~ 1.30 m depth (e.g., increase in common inner shelf genera, like *Bulimina* and
422 *Bolivina*, and agglutinated taxa) indicate the beginning of a transition to open marine/inner shelf
423 sediments. This section contains two carbon dates at approximately the same depth (1.59 m)
424 from mollusk shells, one of which likely contains reworked material because it records an
425 unreasonable age for sediments filling a Holocene estuary ($41,030 \pm 1,703$ cal yrs B.P.). The
426 other date provides an age of $7,787 \pm 136$ cal yr B.P. for the outer bay sediments. The upper 1 m
427 section of PC-4 also consisted of material not suitable for sampling likely containing
428 unconsolidated, unstratified inner shelf deposits that became mixed during retrieval. While
429 fragmentation of tests appears low throughout the core, there is a slight increase in the number of
430 fragments in the outer bay section of the core, indicating a higher energy environment.

431

432 4.3 Gravity core 6

433 Along the eastern edge of the paleovalley, GC-6 penetrated bright seismic reflectors that are
434 represented in the core as a ~ 0.8 m sandy package of sediments atop medium-gray estuarine
435 sediments (Figure 9A). Starting at the base of GC-6, clay sediments are dominated by *Ammonia*,

436 indicating a central bay environment dated to $8,367 \pm 181$ Cal yrs B.P. (mollusk at ~2.1 m
437 depth). These central bay sediments transition to outer bay, as indicated by an increase in
438 *Elphidium* at ~1.7 m depth, with an approximate age of 8.2 ka based on the age model (Figure
439 9B). Smaller sandy intervals at the top of the outer bay sediments provide mollusk carbon dates
440 of $7,709 \pm 147$ Cal yr B.P. and $7,760 \pm 142$ Cal yr B.P. preceding an irregular contact with the
441 sandy package of sediments (Figure 9B). Shell fragments decrease in abundance going up the
442 core, while foraminifer test fragmentation increases going up the core, potentially indicating that
443 the sandy package contains reworked material. A mollusk shell within the sandy package was
444 dated to $4,319 \pm 165$ Cal yrs B.P. and foraminifera within the sandy package indicate a transition
445 from outer bay to inner shelf was taking place until the uppermost sample (GC-6 7-8.5). This
446 uppermost sample contained a foram assemblage that did not match any other assemblages in the
447 study area. It was compared to modern foraminifera assemblages obtained by Phleger (1965)
448 from Galveston Lagoon on Galveston Island, and two grab samples taken from within the flood-
449 and ebb-tidal areas of Bolivar Roads tidal inlet by the MGG 2018 Field Course (Figure 10,
450 Appendix A). A similar method of foram assemblage comparison was used by Hawkes and
451 Horton (2012) to identify inner shelf-sourced washover sediments from Hurricane Ike on
452 Galveston and San Luis Islands. Our GC-6 comparison revealed that the uppermost sample most
453 closely resembles Phleger's Station 11 sample from Galveston Lagoon (Figure 10). However, the
454 sample does not contain a higher amount of plant debris as would be expected in a back-barrier
455 marsh environment. As a result, the lower portion of the sandy package is interpreted as
456 transgressive lag capped by probable washover deposits, rather than a relict drowned barrier
457 island.

458

459 4.4 Gravity cores 4 and 5

460 GC-4 and GC-5 represent a composite section sampling two different seismic facies along the
461 same seismic line, both of which contain central bay sediments (Figure 11 & 12). GC-4, which
462 penetrates the older seismic facies, is unique in that it contains the lowest populations of
463 foraminifera of all the cores. All samples obtained from GC-4 contain less than 100 individuals,
464 and sections of the core are barren of foraminifera (Figure 11B). Situated on the western edge of
465 the paleovalley (Figure 11A), GC-4 primarily consists of medium-gray clay with a relatively
466 higher amount of organic material (Figure 6d), lower amount of shell fragments, and more
467 visible burrowing. The base of the core contains a barren section, which is interpreted as bay
468 margin deposits, and organic material at 3.35 m depth was dated to $8,470 \pm 144$ cal yr B.P. These
469 deposits transition to central bay sediments dominated by *Ammonia* and *Elphidium* with
470 decreased organic material and increased burrowing and shell fragments (Figure 11B). The age
471 model for this core (Figure 11B) indicates the transition took place ~ 8.3 ka. Above the central
472 bay sediments, the core transitions back to barren deposits characterized by burrows and organic
473 material at 0.82 m depth dated to $7,977 \pm 221$ cal yr B.P. and the age model dates the transition
474 at ~ 1.4 m depth to ~ 8.1 ka. The upper section of the core contains a thin sand interval with
475 organic material at 0.56 m dated to $7,913 \pm 255$ cal yrs B.P. and is capped by a section of silty
476 sediments. The foraminiferal assemblage in this section is dominated by *Ammonia* and
477 *Elphidium* with a slight increase in agglutinated and common inner shelf taxa indicating a
478 transition to outer bay and then inner shelf deposits.

479

480 GC-5, which penetrated the younger seismic facies in this two-core composite section, contains
481 central bay sediments capped by outer bay deposits (Figure 12). The base of GC-5 contains

482 medium-gray clay with shell fragments, and a single burrow (Figure 6e). Shell material in this
483 section (2.92 m depth) was dated to $8,467 \pm 130$ cal yr B.P. and foraminifera are dominated by
484 *Ammonia*. The age model (Figure 12B) indicates the central bay to outer bay transition occurred
485 ~ 8.4 ka. The outer bay sediments are comprised of medium-gray clay containing sporadic 2-4
486 cm-scale sandy layers that thicken toward the top of the core to decimeter scale layers with more
487 shell fragments. The upper portion of the core also contains a peak in foram fragmentation and is
488 dominated by *Elphidium*. Increasing diversity and presence of agglutinated forams from 1.0 m
489 depth to the top of the core indicate an outer bay depositional environment transitioning to
490 modern day marine inner shelf. The peak in fragmentation at approximately 1.0 m depth
491 coincides with a peak in dominance of *Ammonia* and suggests that the increase in *Ammonia*
492 likely represents reworked material. The outer bay section was dated to $8,445 \pm 135$ cal yr B.P.
493 at 2.50 m depth and $6,661 \pm 169$ cal yr B.P. near the top at 0.73 m depth.

494

495 4.5 Gravity core 1

496 GC-1 is an extremely short (0.35 m) core (Figure 6h). Its location was selected to investigate
497 dipping reflectors seen in seismic data hypothesized to be a Holocene-aged point bar deposit
498 from a tributary at the edge of the Trinity Paleovalley (Figure 13). Instead, the core penetrated a
499 Pleistocene-age terrace containing sticky, dense, burrowed Beaumont Clay. This clay is capped
500 by burrowed sand and thick shell hash and has a sharp contact with modern inner shelf deposits
501 at approximately 0.14 m depth (Figure 13B). Foraminiferal analysis revealed a large population
502 of foraminifera, dominated by *Elphidium*, within one of the burrows of the terrace. Carbon
503 dating of these foraminifera tests revealed an age of $38,081 \pm 1,833$ cal yr B.P. almost certainly
504 owing to the inclusion of older material, potentially in the form of dissolved inorganic carbon

505 from the Beaumont Formation. Samples at the terrace contact contained lower populations of
506 foraminifera dominated by *Ammonia*. Sediments above the terrace were dominated by both
507 *Elphidium* and *Ammonia* with a slight increase in agglutinated forams and a more significant
508 increase in inner shelf genera, indicating a transition to a modern marine environment. Two
509 radiocarbon ages were obtained from approximately the same interval in the core (0.05 m depth)
510 as a method of comparing ages from foraminifera tests and mollusk shells. The foraminifera
511 provided an older age of $1,753 \pm 143$ cal yr B.P. than the mollusk shell, which was dated to 589
512 ± 97 cal yr B.P. The difference in the ages may indicate an amalgamation of material in a
513 condensed section on the sediment-starved modern shelf, the presence of sediments containing
514 detrital carbonate within the foram tests resulting in an older age, or perhaps diagenetic alteration
515 of the foram tests, with recrystallization of pore water carbonate incorporating older material on
516 the foraminifer tests, which have a higher surface to mass ratio than the mollusk shells.
517 Regardless, both ages indicate a much younger age for the 14 cm thick open shelf deposit
518 (Figure 13B) than any of the estuary sediments in the river valley. A spike in fragmentation of
519 foram tests coincides with the contact between the terrace and modern deposition, indicating a
520 more significant amount of reworking at the contact. Seismic data at this location show
521 prominent draping of sediments along the edges of the terrace (Figure 13A).

522

523 4.6 Gravity core 2

524 GC-2's location was chosen to identify a set of dipping reflectors believed to be part of a paleo-
525 tidal-delta (Figure 14A). The core consists primarily of medium-gray clay with numerous layers
526 of silty sand (Figure 6f). The lower part of the core contains foraminifera approximating 50-50
527 *Ammonia* and *Elphidium*. This assemblage combined with the increased sand content and the

528 relatively higher percent of foram test fragmentation indicate this section likely contains tidal
529 delta deposits. Because it is capped by a less-sandy section dominated by *Elphidium* indicating
530 an outer bay environment, the base of the core is interpreted as a flood-tidal delta. Carbon dates
531 obtained near the transition from tidal delta to outer bay provide ages of $8,445 \pm 135$ cal yr B.P.
532 from a mollusk shell at 2.07 m depth and $8,546 \pm 173$ cal yr B.P. also from a mollusk shell at
533 2.19 m depth. The top of the core contains a spike in *Ammonia* coupled with an increase in
534 fragmentation. Similar to GC-5, coincident increase in fragmentation with a spike in *Ammonia*
535 likely represent a reworking of central bay material in the outer bay environment. The top of the
536 core contains a transition to modern inner shelf deposition at ~ 7.0 ka, represented by the increase
537 in diversity and presence of agglutinated foraminifera at ~ 0.5 m depth.

538

539 **5. Discussion**

540 The coring locations in this study were chosen to sample specific seismic facies and were not
541 intended to provide a cross-section down the Holocene estuary. However, the data can provide
542 several short cross sections along strike in the proximal, middle, and distal parts of our study
543 area. Together, these cross sections provide a composite picture of the nature and timing of
544 environmental change across this part of the estuary from its initial flooding ~ 10 ka to its
545 continued evolution by ~ 6 ka. A cross section analysis of the cores across the incised valley
546 combined with interpolated ages from the age models shows consistent paleoenvironmental
547 changes across multiple cores (Figure 15). PC-2 and PC-4 do not transition from upper bay to
548 central bay environments at the same time, likely due to the elevation of the Pleistocene terrace
549 at PC-4's location. However, PC-2, PC-4, and GC-6 all transition from central bay to outer bay
550 environments at approximately the same time – 8.2-8.0 ka. Shortly after this change, GC-4

551 transitions to an outer bay environment at ~7.9 ka, and outer bay sediments thicken in the cores
552 moving seaward from PC-2. Similarly, GC-2 and GC-5 show a coincident transition to outer bay
553 environment at ~8.4 ka (Figure 15).

554
555 Additionally, all cores in the study area, except for GC-6, appear to transition to an inner shelf
556 environment by ~6.0 ka, although this interval is difficult to date because of the likely erosion of
557 material during transgression and the limited upper seafloor sediments observed in all cores
558 (Figure 16). This coincident timing suggests that the paleoestuary was stable and changes in
559 shoreline position and/or lateral shifts in the position of the tidal inlet led to the observed
560 environmental transitions. Overall, the lateral differences in sediments within the cores reflect
561 contemporaneous estuarine environmental variability.

562
563 Micropaleontologic evidence from these cores confirm the existence of a long-term stable
564 estuarine environment; however, the seaward boundary of this estuary differs from previous
565 studies (Figure 17). Approximately 9.8-9.6 ka, a large estuary stretched from the modern
566 shoreline of Galveston Bay to seaward of Heald Bank. The flood-tidal delta at the base of GC-2
567 combined with the 8.7 ka age of the transgressive ravinement identified by Thomas and
568 Anderson (1994) indicates the shoreline shifted landward of Heald Bank by at least 8.8 ka. This
569 finding is inconsistent with the interpretation by Rodriguez et al. (2004) that the paleoestuary
570 extended to seaward of Heald Bank until 7.7 ka. Our data indicate the paleoestuary was stable
571 landward of Heald Bank for ~2 kyr with some tidal inlet changes that altered the environment
572 within the estuary without transgressing the shoreline (Figure 17). A subsequent landward shift
573 took place ~6.9 ka when the barrier system transgressed to a location between GC-2 and GC-5.

574 By ~6.0 ka the locations of almost all cores in the study area transitioned to inner shelf
575 environments. Washover deposits in GC-6 combined with inner shelf environment of the cores,
576 indicate the shoreline was landward of the study area, but did not reach its modern location until
577 ~2.5 ka when Bolivar Peninsula began to prograde calling into question the interpretation of
578 Galveston Island forming as early as 5.3 ka (Rodriguez et al., 2004).

579

580 5.1 *Stable paleoestuary*

581 Research conducted by the Anderson group argues for the existence of >75 km long paleoestuary
582 from Heald Bank ~50 km offshore Galveston Bay to the modern bay between ~8.2-7.8 ka
583 (Figure 1) (Anderson et al., 2008; Rodriguez et al., 2004). This evidence includes seismic data
584 and carbon dating of sediment cores from within modern Galveston Bay and Heald Bank
585 (Anderson et al., 2008; Rodriguez et al., 2004).

586

587 Our data support the long-term stability of the estuary system during this interval, but not the
588 extension of the estuary all the way to Heald Bank. Foraminiferal analysis from PC-2 and PC-4
589 indicates that both sites were located in the central bay from at least 8.8 ka to 8.0 ka, although
590 PC-2 transitioned to a central bay environment by ~9.6 ka, confirming the existence of a long-
591 term stable estuary (Figures 7 & 8). Foraminiferal assemblages in PC-2 and PC-4 during this
592 time period were dominated by *Ammonia* with a secondary presence of *Elphidium*,
593 corresponding to a central bay depositional environment. Assemblages in PC-4 moving up
594 through the core show a decreasing abundance of *Ammonia* and an increase in *Elphidium* over
595 time indicating a gradual environmental transition from upper bay to central bay and to outer
596 bay. However, higher resolution analysis of PC-2 shows fluctuations in *Ammonia* and *Elphidium*

597 abundances throughout the entire central bay interval, which may correspond to salinity
598 fluctuations within the Holocene estuary as tidal inlets changed shape and/or location, or perhaps
599 as precipitation in the catchment varied. Additionally, many of the peaks in *Ammonia* correspond
600 to small increases in foram fragmentation, which may indicate reworking of central bay material
601 during that interval. The PC-2 analysis indicates that portions of the estuary experienced marine
602 mixing ~8.4 ka coinciding with a transition of seaward core locations to outer bay environments.
603 Increased marine influence on the estuary may provide an explanation for the small variations in
604 foraminiferal assemblages observed in the middle estuary.

605
606 GC-4 is located at the western edge of the paleovalley and contains sediment and foraminiferal
607 assemblages that record lateral variation in the boundary of the estuary between ~8.2 ka and ~8.1
608 ka (Figure 11 and 15). While it is difficult to pinpoint the exact forcing mechanism for this
609 expansion with existing evidence, the coincident timing of this flooding of boundaries and the
610 environmental transition in GC-6 show that the outer western boundary of the paleoestuary
611 flooded due to sea-level rise prior to probable partial barrier collapse and the transition to an
612 outer bay seen first in GC-6 and subsequently in PC-2 and PC-4 (Figure 15). Although this
613 flooding may have impacted the stability of the barrier system, it is unlikely that the shoreline
614 changed significantly because GC-2 maintained an outer bay environment during this time
615 (Figure 14), as well as the existence of tidal delta deposits identified by Thomas and Anderson
616 (1994) (Figure 17). However, this hypothesis would require further analysis of high-resolution
617 seismic data as well as additional coring and carbon dating to constrain the extent of the
618 paleoestuary flooding.

619

620 5.2 *Paleoshoreline changes*

621 Rodriguez et al. (2004) describe estuarine muds in Heald Bank cores that were dated to $8,015 \pm$
622 50 and $7,770 \pm 65$ yr ago and suggested that the outer boundary of the paleoestuary was seaward
623 of Heald Bank until ~ 7.77 ka. Due to the lack of preservation of barrier islands offshore in the
624 sediment record, we must infer original island locations or areas of development based on the
625 data that are preserved. Tidal inlet and tidal delta deposits are considered evidence for the
626 presence of barrier systems that are not preserved (Anderson et al., 2016). Analysis of GC-2
627 reveals the existence of flood tide delta deposits dated to before ~ 8.5 ka, indicating that the inlet
628 (and thus the barrier island system) was nearby and well landward of Heald Bank (Figure 14).
629 Likewise, the presence of washover deposits in GC-5 at ~ 6.7 ka and GC-6 at ~ 4.3 ka
630 demonstrates the landward migration of the paleoshoreline as sea level continued to rise
631 throughout the Holocene (Figure 17). Both GC-2 and GC-5 transition to outer bay environments
632 by ~ 8.4 ka (Figures 12 & 14), indicating that the outer boundary of the estuary shifted prior to
633 the transition to what Rodriguez et al. (2004) describe as shoreface deposits in Heald Bank cores.
634 A microfossil analysis of Heald Bank cores would have confirmed if the “estuarine” sediments
635 described by Rodriguez et al. (2004) originated in an estuarine environment.

636

637 An earlier interpretation by Thomas and Anderson (1994) inferred Heald Bank and other sandy
638 deposits on the Texas shelf to be marine sand banks. Despite their morphological similarities to
639 barrier islands, many modern marine sand banks are not the result of “in-place drowning of
640 barriers” (Snedden and Dalrymple, 1999); rather, they are actively modified marine deposits
641 overlying a transgressive ravinement surface that likely formed from remnant ebb-tidal delta
642 deposits as the shoreline shifted landward (Figure 17) (Dyer and Huntley, 1999; Penland et al.,

643 1988). Based on the seismic interpretation of Thomas and Anderson (1994), Heald Bank formed
644 from re-worked marine sands above a transgressive ravinement formed by erosion of estuarine
645 deposits. The locations of Thomas, Shepard, and Heald Banks coincide with seismic facies
646 interpreted as flood-tidal delta deposits (Thomas and Anderson, 1994), but were more likely to
647 be ebb-tidal delta sediments (Figure 17). These sand banks likely formed as sand ridges off of
648 seafloor irregularities at an angle from the ebb-tidal deltas and were later detached as the ebb-
649 tidal delta was transgressed, providing source material for the sand banks (e.g., Type 2 sand
650 ridges, Dyer and Huntley, 1999). Afterwards, these deposits were continually reworked by
651 coastal currents as modern marine sand banks.

652

653 Sandy deposits in the outer bay sequence of GC-5 are likely washover sediments from a
654 proximal barrier island. The absence of these sands in the bay margin intervals of GC-4 indicate
655 that these washovers are not from the edge of the bay, westward of GC-5's location (Figure 12).
656 We hypothesize that a barrier system developed near GC-5's position ~20 km seaward of the
657 modern shoreline ~6.7 ka (Figure 17). Sandy intervals in the outer bay section of GC-2, located
658 seaward of GC-5, dated to $6,973 \pm 170$ cal yr B.P. also suggest that a barrier had developed
659 nearby in the distal direction, and these sandy intervals could represent paleo-storm washover
660 deposits from that barrier system.

661

662 In addition to the data provided in GC-2 and GC-5, washover deposits in GC-6 (Figure 9)
663 indicate that there was a barrier system proximal to GC-6's location between ~7.4 and 4.3 ka
664 (Figure 17). The upper sample obtained from GC-6 closely resembles a modern marsh
665 assemblage from Galveston Island (see 4.3), indicating that these washovers could be spilled

666 over from either a back-barrier marsh or a marsh located on the edge of the paleoestuary, and are
667 not a remnant ebb-tidal delta deposit (Figure 10).

668
669 Analysis of Galveston Island core data by Rodriguez et al. (2004) coupled with previous research
670 on the island by Berrard et al. (1970) indicate that Galveston Island began prograding ~5.3 ka
671 giving the paleoshoreline an irregular shape and showing rapid, rather than gradual, coastline
672 changes in the past (Figure 1). Although Rodriguez et al. (2004) obtained their own radiocarbon
673 ages, they indicated there was a significant amount of uncertainty in the methods used by Berrard
674 et al. (1970). Excluding the work done by Berrard et al. (1970) leaves a single carbon date
675 obtained by Rodriguez et al. (2004) from older beach ridges on Galveston Island providing an
676 age of ~5.3 ka; this age could come from reworked material. The irregular shape of these
677 paleoshorelines (Figure 1) is likely not representative of coastal changes which would have
678 adjusted to sea-level rise “dynamically while maintaining a characteristic geometry that is unique
679 to a particular coast” (FitzGerald et al., 2008). Based on probable washover sediments reported
680 here, this paleoshoreline likely stepped landward multiple times until reaching its modern-day
681 location by ~2.5 ka and the ~5.3 ka age thus represents reworked sediments. However, the lack
682 of data between our study area and the modern shoreline makes it difficult to constrain this
683 migration beyond its proximity to GC-6 at ~4.3 ka.

684

685 *5.3 Timeline of sea-level rise*

686 A comparison of environmental changes in the paleoestuary and the record of Gulf of Mexico
687 sea-level rise indicates that most of these transitions coincide with or occurred after periods of
688 rapid increases in sea level (Figure 16). A majority of these changes took place when global sea

689 level rise was greater than twice the modern rate ($\sim 15 \text{ mm yr}^{-1}$), although some environmental
690 shifts transpired after global sea level rise slowed significantly, indicating other regional and
691 local changes, such as climate, may have contributed to these transitions (Figure 16).

692
693 Following the retreat of ice from Noble Inlet and Hudson Strait $\sim 9.1 \text{ ka}$ (Jennings et al., 2015),
694 PC-4 transitioned to a central bay environment. The early opening of the Tyrell Sea in North
695 America (now called Hudson Bay) $\sim 8.7 \text{ ka}$ (Jennings et al., 2015) preceded the transitions in
696 GC-2 and GC-5 from central to outer bay as well as a brief increase in diversity in PC-2 that may
697 represent increased marine mixing. The rapid discharge of freshwater from North American
698 glacial lakes, dubbed the “8.2 ka event” that resulted in short-term climate cooling (Cronin et al.,
699 2007; Jennings et al., 2015; Törnqvist et al., 2004; Ullman et al., 2016) coincided with the
700 flooding of the paleoestuary that expanded at least the western boundary visible in GC-4, and the
701 environmental change in GC-6 from central bay to outer bay $\sim 8.2 \text{ ka}$. Following the 8.2 ka event,
702 there was a reduced rate of global sea-level rise (Lambeck et al., 2014). GC-4 resumed a bay
703 margin environment shortly afterwards, around the same time that PC-2 and PC-4 transitioned to
704 outer bay ($\sim 8.1 \text{ ka}$). Glacial ice retreat in the Foxe Basin west of Baffin Island $\sim 7.4 \text{ ka}$ (Jennings
705 et al., 2015) preceded a brief increase in diversity that we observe in GC-5, possibly associated
706 with increased marine mixing due to an unstable barrier system $\sim 7.3 \text{ ka}$. This change also
707 coincides with a regional climate transition from cool/wet to warm/dry (Figure 16) (Weight et
708 al., 2011), which may have contributed to environmental change through decreased precipitation
709 and thus decreased sediment supply to the paleoestuary. GC-2 transitioned from outer bay to
710 inner shelf $\sim 6.9 \text{ ka}$ approximately at the same time as the final deglaciation of the LIS $\sim 6.7 \text{ ka}$
711 (Jennings et al., 2015; Ullman et al., 2016). From 6.7 ka until the onset of recent accelerated sea-

712 level rise (~100-150 yr ago), there was a progressive decrease in the rate of global sea-level rise
713 (Lambeck et al., 2014). During this period, our study area transitioned to an inner shelf
714 environment as the previously stable estuary system rapidly shifted landward (Figure 16),
715 suggesting that climate-driven sediment supply played a significant role in maintaining the
716 stability of the early-middle Holocene estuary and its protective barrier system and a reduction in
717 this sediment supply precipitated retreat. This finding suggests that modern climate warming
718 coupled with human reduced riverine sediment flux may increase the vulnerability of Galveston
719 Island and Bolivar Peninsula in maintaining the modern coastline amid accelerating sea-level
720 rise. The timing of the middle Holocene inner shelf transition is difficult to identify due to the
721 removal of material above the transgressive ravinement with the exception of a single carbon
722 date of a transgressive shell lag in GC-6 constraining probable washover deposits to younger
723 than 4.3 ka.

724

725 *5.4 Minimal modern seafloor sedimentation*

726 The transition to a modern inner shelf environment is difficult to determine due to the limited
727 amount of modern seafloor material and likely erosion and reworking of upper sediments from
728 the transgressive ravinement. Although it appears to have happened slightly earlier in GC-2, it is
729 probable that the study area was an inner shelf environment by ~6.0 ka and the transgression
730 occurred over the period between 7.0 and 6.0 ka. The limited shelf material in the upper areas of
731 each core represent deposition of ~0.01 cm per year, so it is more likely that material is being
732 removed from the upper seafloor regularly.

733

734 The Texas Mud Blanket (TMB) is a large ($\sim 300 \text{ km}^3$) depositional area on the western Gulf
735 Coast between a bathymetric embayment of the ancient Rio Grande and Colorado River deltas
736 containing $\sim 5 \times 10^{11}$ t of sediment (Weight et al., 2011). Weight et al. (2011) approximated mass
737 accumulation rates in the TMB for the Holocene, with highest accumulation occurring from ~ 9
738 ka to ~ 5.5 ka and ~ 3.5 ka to present. The primary sediment source for the 9-5.5 ka period
739 corresponds to the erosion of nearby Brazos and Colorado deltas, and accumulation decreased as
740 these sediment sources were depleted (Weight et al., 2011). The period of ~ 3.5 ka to present
741 accounts for 57% of total volume accumulation in the TMB, which is attributed to increased
742 efficiency of marine longshore current, specifically the Louisiana-Texas Coastal Current,
743 bringing sediments from as far as the Mississippi River delta (Weight et al., 2011). It is likely
744 that the same mechanism has depleted inner shelf sediments offshore Galveston Bay resulting in
745 minimal modern seafloor sediments in our cores with sediment delivered to regions farther west
746 along the Texas Coast including the TMB.

747

748 **6. Conclusion**

749 We revise the established Holocene coastal change model for the Trinity River incised valley
750 based on new radiocarbon dates and micropaleontological analysis of sediment cores from
751 offshore Galveston Bay, Texas. This study provides environmental context to previous research
752 that primarily utilized seismic and sedimentological analyses revealing consistent environmental
753 changes across multiple cores due to external sea-level rise and climate forcing. As a result of
754 this analysis, we reached the following conclusions:

- 755 • The barrier system was inshore of the modern position of Heald Bank prior to 8.5 ka with
756 landward migration occurring in steps of barrier collapse and stabilization resulting in

757 limited disruption during estuarine environmental transitions. It is unlikely that the
758 shoreline migrated asymmetrically as previously hypothesized, but rather stepped
759 landward in a pattern that approximates the geometry of the modern shoreline.

- 760 • Heald Bank, along with other sand banks along the Texas coast, is likely a marine sand
761 bank developed above the transgressive ravinement from re-worked material after the
762 shoreline shifted prior to 8.5 ka. The development of this marine sand body possibly
763 began in connection with ebb-tidal delta deposits and is not a remnant or drowned barrier
764 island.
- 765 • The Holocene estuary was stable for approximately 2 kyr (~6.9-8.8 ka) during which
766 time the environment experienced minor, but noticeable, perturbations likely due to
767 lateral variations in tidal inlets or partial collapse of barrier systems.
- 768 • Probable washover sediments in multiple cores approximate the location of barrier
769 islands as they migrated landward at ~7-6.7 ka and after ~4.3 ka. The lack of data
770 between our study area and the modern shoreline precludes our ability to map the
771 migration of the barrier system beyond these approximations.
- 772 • Environmental changes within the Holocene estuary coincide with or follow glacial
773 meltwater events from the LIS, with a majority of changes in the estuary occurring during
774 the phase of more accelerated sea level rise in the early Holocene. As the rate sea level
775 rise began to slow due to the final deglaciation of the LIS, additional probable regional
776 hydroclimate forcing affecting the sediment supply resulted in continued environmental
777 change shifting the estuary landward to its modern location.

- 778 • All cores in the study area contain minimal modern seafloor sediments likely due to
779 erosion from the transgressive ravinement and re-working of sediment from ocean
780 currents contributing to the Texas Mud Blanket.

781

782 **7. Data Availability**

783 Datasets related to this article can be found at <https://www.ncei.noaa.gov/access/paleo->
784 [search/study/34592](https://www.ncei.noaa.gov/access/paleo-search/study/34592), an open-source online data repository hosted at NOAA's National Center
785 for Environmental Information.

786

787 **Conflict of Interest**

788 The authors declare no conflict of interest.

789

790 **8. Acknowledgments**

791 This project was funded by the Bureau of Ocean Energy Management under Cooperative
792 Agreement M16AC00020, and the Martin B. Lagoe Micropaleontology Fellowship from the
793 Jackson School of Geosciences at the University of the Texas at Austin. We would like to thank
794 Gabriela Gutierrez, Daniel Duncan, Marcy Davis, the crew of the R/V *Brooks McCall*, TDI
795 Brooks, the class of the 2018 Marine Geology and Geophysics Field Course, and the crew of the
796 R/V *Manta* for their collective assistance in collecting the piston and gravity cores and additional
797 chirp data for this study. We would also like to thank the National Ocean Sciences Accelerator
798 Mass Spectrometry at Woods Hole Oceanographic Institute (NSF Cooperative Agreement
799 number OCE-0753487) for processing our radiocarbon samples, and the Gulf of Mexico
800 Sedimentology Working Group for discussions contributing to the analysis presented in this

EarthArXiv pre-print – this manuscript is not peer-reviewed

801 paper. We acknowledge that research on this project was conducted at the University of Texas at
802 Austin on the Indigenous lands of Turtle Island, on land originally cared for by the Alabama-
803 Coushatta, Caddo, Carrizo/Comerudo, Coahuiltecan, Comanche, Kickapoo, Lipan Apache,
804 Tonkawa, and Ysleta del Sur Pueblo people, many of whom were forcibly removed from their
805 home. For more information about ancestral land you occupy, please visit <https://native-land.ca/>.
806 This is University of Texas Institute for Geophysics Contribution #XXXX.

807
808 **Tables**

809 Table 1. List of radiocarbon dating samples and their calibrated ages.

No.	NOSAMS OS No.	Sample	Type	Process	Calibrated Age	
					Age (yr)	Error (\pm yr)
1	155814	PC-2-S3-7-8.5	Mollusc	Hydrolysis	7,441	127
2	152146	PC-2-S3-82-83.5	Mollusc	Hydrolysis	7,800	134
3	152138	PC-2-S2-69.5-71	Mollusc	Hydrolysis	8,468	135
4	152145	PC-2-S2-100.5-102	Mollusc	Hydrolysis	8,815	175
5	155815	PC-2-S1-14-16	Mollusc	Hydrolysis	9380	133
6	155816	PC-2-S1-23-25	Mollusc	Hydrolysis	9,420	124
7	155817	PC-2-S1-102-104	Mollusc	Hydrolysis	9,794	215
8	155818	PC-4-S3-58.5-60	Mollusc	Hydrolysis	7,787	136
9	152148	PC-4-S3-59	Mollusc	Hydrolysis	41,030	1,703
10	155819	PC-4-S2-15-16.5	Mollusc	Hydrolysis	8,815	175
11	152147	PC-4-S2-94-96	Mollusc	Hydrolysis	9,131	158
12	155820	GC-1-S1-4-6	Foraminifera	Hydrolysis	1,753	143

13	152314	GC-1-S1-5-6	Mollusc	Hydrolysis	589	97
14	152315	GC-1-S1-28.5-30	Foraminifera	Hydrolysis	38,081	1,833
15	155821	GC-2-S1-A-59-61	Mollusc	Hydrolysis	6,973	170
16	152310	GC-2-S2-144-145	Mollusc	Hydrolysis	8,445	135
17	152316	GC-2-S3-6-10	Mollusc	Hydrolysis	8,546	173
18	155902	GC-4-S1-55.5-56.5	Charcoal	Combustion	7,913	255
19	152149	GC-4-S2-13-13.5	Charcoal	Combustion	7,977	221
20	155903	GC-4-S3-120-122	Charcoal	Combustion	8,470	144
21	155822	GC-5-S2-3-5	Mollusc	Hydrolysis	6,661	169
22	155823	GC-5-S3-32-37.5	Mollusc	Hydrolysis	8,445	135
23	155824	GC-5-S3-74-76	Mollusc	Hydrolysis	8,467	130
24	155825	GC-6-S1-11-14	Mollusc	Hydrolysis	>Modern	
25	155826	GC-6-S1-64.5-66	Mollusc	Hydrolysis	4,329	165
26	157505	GC-6-S1-111.5-113	Mollusc	Hydrolysis	7,760	142
27	157506	GC-6-S1-130-131.5	Mollusc	Hydrolysis	7,709	147
28	157511	GC-6-S2-71-72.5	Mollusc	Hydrolysis	8,367	181

810

811 **9. References**

812 Abdulah, K.C., Anderson, J.B., Snow, J.N., Holdford-Jack, L., 2004. The Late Quaternary
813 Brazos and Colorado Deltas, Offshore Texas, U.S.A.—Their Evolution and the Factors
814 that Controlled Their Deposition.

815 Al Mukaimi, M.E., Dellapenna, T.M., Williams, J.R., 2018. Enhanced land subsidence in
816 Galveston Bay, Texas: Interaction between sediment accumulation rates and relative sea
817 level rise. *Estuar. Coast. Shelf Sci.* 207, 183–193.
818 <https://doi.org/10.1016/j.ecss.2018.03.023>

819 Anderson, J.B., Rodriguez, A.B., Milliken, K.T., Taviani, M., 2008. The Holocene evolution of
820 the Galveston estuary complex, Texas: Evidence for rapid change in estuarine

- 821 environments, in: Special Paper 443: Response of Upper Gulf Coast Estuaries to
822 Holocene Climate Change and Sea-Level Rise. Geological Society of America, pp. 89–
823 104. [https://doi.org/10.1130/2008.2443\(06\)](https://doi.org/10.1130/2008.2443(06))
- 824 Anderson, J.B., Wallace, D.J., Simms, A.R., Rodriguez, A.B., Milliken, K.T., 2014. Variable
825 response of coastal environments of the northwestern Gulf of Mexico to sea-level rise
826 and climate change: Implications for future change. *Mar. Geol.* 352, 348–366.
- 827 Anderson, J.B., Wallace, D.J., Simms, A.R., Rodriguez, A.B., Weight, R.W.R., Taha, Z.P., 2016.
828 Recycling sediments between source and sink during a eustatic cycle: Systems of late
829 Quaternary northwestern Gulf of Mexico Basin. *Earth-Sci. Rev.* 153, 111–138.
- 830 Bamber, J.L., Oppenheimer, M., Kopp, R.E., Aspinnall, W.P., Cooke, R.M., 2019. Ice sheet
831 contributions to future sea-level rise from structured expert judgment. *Proc. Natl. Acad.*
832 *Sci.* 116, 11195–11200. <https://doi.org/10.1073/pnas.1817205116>
- 833 Bernstein, A., Gustafson, M.T., Lewis, R., 2019. Disaster on the horizon: The price effect of sea
834 level rise. *J. Financ. Econ.* 134, 253–272. <https://doi.org/10.1016/j.jfineco.2019.03.013>
- 835 Blaauw, M., Christen, J.A., 2011. Flexible paleoclimate age-depth models using an
836 autoregressive gamma process. *Bayesian Anal.* 6, 457–474. <https://doi.org/10.1214/11-BA618>
- 837
- 838 Brenner, O.T., Moore, L.J., Murray, A.B., 2015. The complex influences of back-barrier
839 deposition, substrate slope and underlying stratigraphy in barrier island response to sea-
840 level rise: Insights from the Virginia Barrier Islands, Mid-Atlantic Bight, U.S.A.
841 *Geomorphology* 246, 334–350. <https://doi.org/10.1016/j.geomorph.2015.06.014>
- 842 Burstein, J., Goff, J.A., Gulick, S., Lowery, C., Standring, P., Swartz, J., 2021. Tracking Barrier
843 Island Response to Early Holocene Sea-level Rise: High Resolution Study of Estuarine
844 Sediments in the Trinity River Paleovalley.
- 845 Buzas, M.A., 1990. Another look at confidence limits for species proportions. *J. Paleontol.* 2.
- 846 Cronin, T.M., Vogt, P.R., Willard, D.A., Thunell, R., Halka, J., Berke, M., Pohlman, J., 2007.
847 Rapid sea level rise and ice sheet response to 8,200-year climate event. *Geophys. Res.*
848 *Lett.* 34. <https://doi.org/10.1029/2007GL031318>
- 849 Culver, S.J., 1988. New Foraminiferal Depth Zonation of the Northwestern Gulf of Mexico.
850 *PALAIOS* 3, 69–85. <https://doi.org/10.2307/3514545>
- 851 Davis, R.A., Hayes, M.O., 1984. What is a wave-dominated coast? *Mar. Geol., Hydrodynamics*
852 *and Sedimentation in Wave-Dominated Coastal Environments* 60, 313–329.
853 [https://doi.org/10.1016/0025-3227\(84\)90155-5](https://doi.org/10.1016/0025-3227(84)90155-5).
- 854 Delapenna, T.M., Cardenas, A., Johnson, K., Flocks, J., 2009. Report of the Sand Source
855 Investigation of the Paleo-Sabine-Trinity Marine Features. Texas A&M University
856 Galveston.
- 857 Dutton, A., Carlson, A.E., Long, A.J., Milne, G.A., Clark, P.U., DeConto, R., Horton, B.P.,
858 Rahmstorf, S., Raymo, M.E., 2015. Sea-level rise due to polar ice-sheet mass loss during
859 past warm periods. *Science* 349. <https://doi.org/10.1126/science.aaa4019>

- 860 Dyer, K.R., Huntley, D.A., 1999. The origin, classification and modelling of sand banks and
861 ridges. *Cont. Shelf Res.* 19, 1285–1330. [https://doi.org/10.1016/S0278-4343\(99\)00028-X](https://doi.org/10.1016/S0278-4343(99)00028-X)
- 862 FitzGerald, D.M., Fenster, M.S., Argow, B.A., Buynevich, I.V., 2008. Coastal Impacts Due to
863 Sea-Level Rise. *Annu. Rev. Earth Planet. Sci.* 36, 601–647.
864 <https://doi.org/10.1146/annurev.earth.35.031306.140139>
- 865 Phleger, F., 1960. Sedimentary patterns of microfaunas in northern Gulf of Mexico 34, 267–301.
- 866 Fruergaard, M., Møller, I., Johannessen, P.N., Nielsen, L.H., Andersen, T.J., Nielsen, L., Sander,
867 L., Pejrup, M., 2015. Stratigraphy, Evolution, and Controls of A Holocene
868 Transgressive–Regressive Barrier Island Under Changing Sea Level: Danish North Sea
869 Coast. *J. Sediment. Res.* 85, 820–844. <https://doi.org/10.2110/jsr.2015.53>
- 870 Gehrels, W.R., 2013. Microfossil-Based Reconstruction of Holocene Relative Sea-Level
871 Change. *Sea Level Stud.*
- 872 Goff, J.A., Allison, M.A., Gulick, S.P.S., 2010. Offshore transport of sediment during cyclonic
873 storms: Hurricane Ike (2008), Texas Gulf Coast, USA. *Geology* 38, 351–354.
874 <https://doi.org/10.1130/G30632.1>
- 875 Goff, J.A., Flood, R.D., Austin, Jr., James A., Schwab, W.C., Christensen, B., Browne, C.M.,
876 Denny, J.F., Baldwin, W.E., 2015. The impact of Hurricane Sandy on the shoreface and
877 inner shelf of Fire Island, New York: Large bedform migration but limited erosion. *Cont.*
878 *Shelf Res.* 98, 13–25. <https://doi.org/10.1016/j.csr.2015.03.001>
- 879 Haslett, J., Parnell, A., 2008. A simple monotone process with application to radiocarbon-dated
880 depth chronologies. *J. R. Stat. Soc. Ser. C Appl. Stat.* 57, 399–418.
881 <https://doi.org/10.1111/j.1467-9876.2008.00623.x>
- 882 Hawkes, A.D., Horton, B.P., 2012. Sedimentary record of storm deposits from Hurricane Ike,
883 Galveston and San Luis Islands, Texas. *Geomorphology* 171–172, 180–189.
884 <https://doi.org/10.1016/j.geomorph.2012.05.017>
- 885 Heaton, T.J., Köhler, P., Butzin, M., Bard, E., Reimer, R.W., Austin, W.E.N., Ramsey, C.B.,
886 Grootes, P.M., Hughen, K.A., Kromer, B., Reimer, P.J., Adkins, J., Burke, A., Cook,
887 M.S., Olsen, J., Skinner, L.C., 2020. Marine20—The Marine Radiocarbon Age
888 Calibration Curve (0–55,000 cal BP). *Radiocarbon* 62, 779–820.
889 <https://doi.org/10.1017/RDC.2020.68>
- 890 Horton, B.P., R.E. Kopp, A. Dutton, T.A. Shaw, 2019. Geological records of past sea-level
891 changes as constraints for future projections. *Past Glob. Chang. Mag.* 27.
892 <https://doi.org/10.22498/pages.27.1.28>
- 893 IPCC, 2021: Summary for Policymakers. In: *Climate Change 2021: The Physical Science Basis.*
894 *Contribution of Working Group I to the Sixth Assessment Report of the*
895 *Intergovernmental Panel on Climate Change* [MassonDelmotte, V., P. Zhai, A. Pirani,
896 S.L. Connors, C. Péan, S. Berger, N. Caud, Y. Chen, L. Goldfarb, M.I. Gomis, M.
897 Huang, K. Leitzell, E. Lonnoy, J.B.R. Matthews, T.K. Maycock, T. Waterfield, O.
898 Yelekçi, R. Yu, and B. Zhou (eds.)]. Cambridge University Press. In Press.

- 899 Jennings, A., Andrews, J., Pearce, C., Wilson, L., Ólfasdóttir, S., 2015. Detrital carbonate peaks
900 on the Labrador shelf, a 13–7ka template for freshwater forcing from the Hudson Strait
901 outlet of the Laurentide Ice Sheet into the subpolar gyre. *Quat. Sci. Rev.* 107, 62–80.
902 <https://doi.org/10.1016/j.quascirev.2014.10.022>
- 903 Kirwan, M.L., Megonigal, J.P., 2013. Tidal wetland stability in the face of human impacts and
904 sea-level rise. *Nature* 504, 53–60. <https://doi.org/10.1038/nature12856>
- 905 K.T. Milliken, J.B. Anderson, A.B. Rodriguez, 2008. A new composite Holocene sea-level curve
906 for the northern Gulf of Mexico., in: *Response of Upper Gulf Coast Estuaries to*
907 *Holocene Climate Change and Sea Level Rise*, Geological Society of America Special
908 Paper 443. pp. 1–11.
- 909 Lambeck, K., Rouby, H., Purcell, A., Sun, Y., Sambridge, M., 2014. Sea level and global ice
910 volumes from the Last Glacial Maximum to the Holocene. *Proc. Natl. Acad. Sci.* 111,
911 15296–15303. <https://doi.org/10.1073/pnas.1411762111>
- 912 Lentz, E.E., Hapke, C.J., Stockdon, H.F., Hehre, R.E., 2013. Improving understanding of near-
913 term barrier island evolution through multi-decadal assessment of morphologic change.
914 *Mar. Geol.* 337, 125–139. <https://doi.org/10.1016/j.margeo.2013.02.004>
- 915 Lorenzo-Trueba, J., Ashton, A.D., 2014. Rollover, drowning, and discontinuous retreat: Distinct
916 modes of barrier response to sea-level rise arising from a simple morphodynamic model.
917 *J. Geophys. Res. Earth Surf.* 119, 779–801. <https://doi.org/10.1002/2013JF002941>
- 918 Miller, M.M., Shirzaei, M., 2021. Assessment of Future Flood Hazards for Southeastern Texas:
919 Synthesizing Subsidence, Sea-Level Rise, and Storm Surge Scenarios. *Geophys. Res.*
920 *Lett.* 48, e2021GL092544. <https://doi.org/10.1029/2021GL092544>
- 921 Moore, L.J., List, J.H., Williams, S.J., Stolper, D., 2010. Complexities in barrier island response
922 to sea level rise: Insights from numerical model experiments, North Carolina Outer
923 Banks. *J. Geophys. Res. Earth Surf.* 115. <https://doi.org/10.1029/2009JF001299>
- 924 NOAA, 2021. Sea Level Trends, National Ocean and Atmospheric Administration.
925 <https://tidesandcurrents.noaa.gov/sltrends/>
- 926 Olson, H.C., Leckie, R.M. (Eds.), 2003. *Micropaleontologic Proxies for Sea-Level Change and*
927 *Stratigraphic Discontinuities*. SEPM (Society for Sedimentary Geology).
928 <https://doi.org/10.2110/pec.03.75>
- 929 Paine, J.G., 1993. Subsidence of the Texas coast: inferences from historical and late Pleistocene
930 sea levels. *Tectonophysics, Geological Perspectives on Global Change* 222, 445–458.
931 [https://doi.org/10.1016/0040-1951\(93\)90363-O](https://doi.org/10.1016/0040-1951(93)90363-O)
- 932 Palermo, R.V., Piliouras, A., Swanson, T.E., Ashton, A.D., Mohrig, D., 2021. The effects of
933 storms and a transient sandy veneer on the interannual planform evolution a low-relief
934 coastal cliff and wave-cut platform at Sargent Beach, Texas, USA. *Earth Surf. Dyn.*
935 *Discuss.* 1–20.
- 936 Penland, S., Boyd, R., Suter, J.R., 1988. Transgressive depositional systems of the Mississippi
937 Delta plain; a model for barrier shoreline and shelf sand development. *J. Sediment. Res.*
938 58, 932–949. <https://doi.org/10.1306/212F8EC2-2B24-11D7-8648000102C1865D>

- 939 Phillips, J.D., Slattery, M.C., Musselman, Z.A., 2004. Dam-to-delta sediment inputs and storage
940 in the lower trinity river, Texas. *Geomorphology* 62, 17–34.
941 <https://doi.org/10.1016/j.geomorph.2004.02.004>
- 942 Phleger, F.B., 1965. Patterns of Marsh Foraminifera, Galveston Bay, Texas. *Limnol. Oceanogr.*
943 10, R169–R184. <https://doi.org/10.4319/lo.1965.10.suppl2.r169>
- 944 Phleger, F.B., 1951. Ecology of Foraminifera, Northwest Gulf of Mexico. Geological Society of
945 America.
- 946 Poag, C.W., 1981. Benthic Foraminifera of the Gulf of Mexico.
- 947 Port of Houston, 2020. Statistics. Port of Houston. <https://porthouston.com/about-us/statistics/>
- 948 Raff, J.L., Shawler, J.L., Ciarletta, D.J., Hein, E.A., Lorenzo-Trueba, J., Hein, C.J., 2018.
949 Insights into barrier-island stability derived from transgressive/regressive state changes of
950 Parramore Island, Virginia. *Mar. Geol.* 403, 1–19.
951 <https://doi.org/10.1016/j.margeo.2018.04.007>
- 952 Ramsey, C.B., 2009. Bayesian Analysis of Radiocarbon Dates. *Radiocarbon* 51, 337–360.
953 <https://doi.org/10.1017/S0033822200033865>
- 954 Rehkemper, L.J., 1969. Sedimentology of Holocene Estuarine Deposits, Galveston Bay 12–52.
- 955 Reimer, P.J., Austin, W.E.N., Bard, E., Bayliss, A., Blackwell, P.G., Ramsey, C.B., Butzin, M.,
956 Cheng, H., Edwards, R.L., Friedrich, M., Grootes, P.M., Guilderson, T.P., Hajdas, I.,
957 Heaton, T.J., Hogg, A.G., Hughen, K.A., Kromer, B., Manning, S.W., Muscheler, R.,
958 Palmer, J.G., Pearson, C., Plicht, J. van der, Reimer, R.W., Richards, D.A., Scott, E.M.,
959 Southon, J.R., Turney, C.S.M., Wacker, L., Adolphi, F., Büntgen, U., Capano, M.,
960 Fahrni, S.M., Fogtmann-Schulz, A., Friedrich, R., Köhler, P., Kudsk, S., Miyake, F.,
961 Olsen, J., Reinig, F., Sakamoto, M., Sookdeo, A., Talamo, S., 2020. The IntCal20
962 Northern Hemisphere Radiocarbon Age Calibration Curve (0–55 cal kBP). *Radiocarbon*
963 62, 725–757. <https://doi.org/10.1017/RDC.2020.41>
- 964 Rodriguez, A.B., Anderson, J.B., Simms, A.R., 2005. Terrace Inundation as an Autocyclic
965 Mechanism for Parasequence Formation: Galveston Estuary, Texas, U.S.A. *J. Sediment.*
966 *Res.* 75, 608–620. <https://doi.org/10.2110/jsr.2005.050>
- 967 Rodriguez, A.B., Anderson, J.B., Siringan, F.P., Taviani, M., 2004. Holocene Evolution of the
968 East Texas Coast and Inner Continental Shelf: Along-Strike Variability in Coastal Retreat
969 Rates. *J. Sediment. Res.* 74, 405–421. <https://doi.org/10.1306/092403740405>
- 970 Ryan, W. B. F., S.M. Carbotte, J. Coplan, S. O'Hara, A. Melkonian, R. Arko, R.A. Weissel, V.
971 Ferrini, A. Goodwillie, F. Nitsche, J. Bonczkowski, and R. Zemsky (2009), Global Multi-
972 Resolution Topography (GMRT) synthesis data set, *Geochem. Geophys. Geosyst.*, 10,
973 Q03014, doi:10.1029/2008GC002332.
- 974 Shawler, J.L., Ciarletta, D.J., Connell, J.E., Boggs, B.Q., Lorenzo-Trueba, J., Hein, C.J., 2021.
975 Relative influence of antecedent topography and sea-level rise on barrier-island
976 migration. *Sedimentology* 68, 639–669. <https://doi.org/10.1111/sed.12798>

- 977 Simms, A.R., Lambeck, K., Purcell, A., Anderson, J.B., Rodriguez, A.B., 2007. Sea-level history
978 of the Gulf of Mexico since the Last Glacial Maximum with implications for the melting
979 history for the Laurentide Ice Sheet. *Quat. Sci. Rev.* 26, 920–940.
- 980 Siringan, F.P., Anderson, J.B., 1993. Seismic facies, architecture, and evolution of the Bolivar
981 Roads tidal inlet/delta complex, East Texas Gulf Coast. *J. Sediment. Res.* 63, 794–808.
982 <https://doi.org/10.1306/D4267C08-2B26-11D7-8648000102C1865D>
- 983 Snedden, J.W., Dalrymple, R.W., 1999. Modern Shelf Sand Ridges: From Historical Perspective
984 to a Unified Hydrodynamic and Evolutionary Model.
- 985 Swartz, J.M., 2019. Channel processes and products in subaerial and submarine environments
986 across the Gulf of Mexico. University of Texas, Austin, Tex.
- 987 Thomas, M.A., Anderson, J.B., 1994. Sea-Level Controls on the Facies Architecture of the
988 Trinity/Sabine Incised-Valley System, Texas Continental Shelf.
- 989 Törnqvist, T.E., Bick, S.J., González, J.L., Borg, K. van der, Jong, A.F.M. de, 2004. Tracking the
990 sea-level signature of the 8.2 ka cooling event: New constraints from the Mississippi
991 Delta. *Geophys. Res. Lett.* 31. <https://doi.org/10.1029/2004GL021429>
- 992 Ullman, D.J., Carlson, A.E., Hostetler, S.W., Clark, P.U., Cuzzone, J., Milne, G.A., Winsor, K.,
993 Caffee, M., 2016. Final Laurentide ice-sheet deglaciation and Holocene climate-sea level
994 change. *Quat. Sci. Rev.* 152, 49–59. <https://doi.org/10.1016/j.quascirev.2016.09.014>
- 995 Vitousek, S., Barnard, P.L., Fletcher, C.H., Frazer, N., Erikson, L., Storlazzi, C.D., 2017.
996 Doubling of coastal flooding frequency within decades due to sea-level rise. *Sci. Rep.* 7,
997 1399. <https://doi.org/10.1038/s41598-017-01362-7>
- 998 Wagner, A.J., Guilderson, T.P., Slowey, N.C., Cole, J.E., 2009. Pre-Bomb Surface Water
999 Radiocarbon of the Gulf of Mexico and Caribbean as Recorded in Hermatypic Corals.
1000 *Radiocarbon* 51, 947–954. <https://doi.org/10.1017/S0033822200034020>
- 1001 Wantland, K.F., 1969. Distribution of Modern Brackish-Water Foraminifera in Trinity Bay 93–
1002 117.
- 1003 Weight, R.W.R., Anderson, J.B., Fernandez, R., 2011. Rapid Mud Accumulation On the Central
1004 Texas Shelf Linked To Climate Change and Sea-Level Rise. *J. Sediment. Res.* 81, 743–
1005 764. <https://doi.org/10.2110/jsr.2011.57>
- 1006 White, W.A., Morton, R.A., Holmes, C.W., 2002. A comparison of factors controlling
1007 sedimentation rates and wetland loss in fluvial–deltaic systems, Texas Gulf coast.
1008 *Geomorphology* 44, 47–66. [https://doi.org/10.1016/S0169-555X\(01\)00140-4](https://doi.org/10.1016/S0169-555X(01)00140-4)
1009

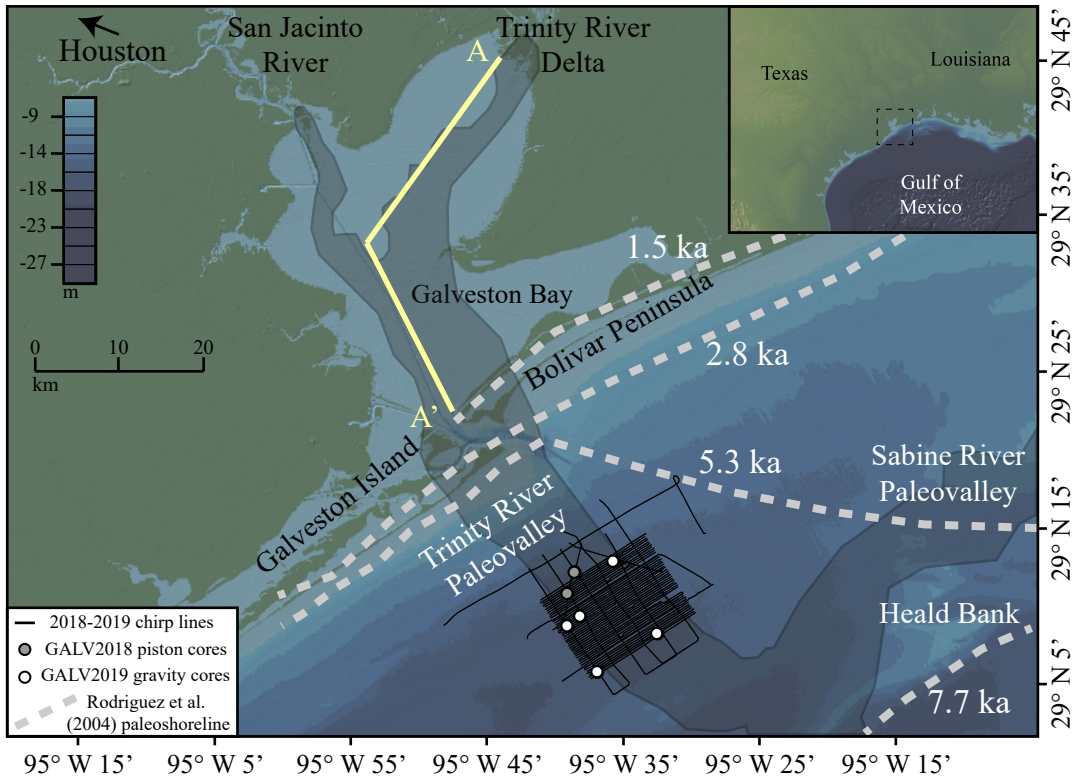


Figure 1. Study area offshore Galveston Bay, Texas, with Trinity River incised valley (gray outline), A-A' profile of cross-section shown in Figure 4 from Anderson et al. (2008), high-resolution seismic lines (black lines), 2018 piston cores (gray circles), 2019 gravity cores (white circles), and paleoshorelines (gray dashed lines) based on interpretation from Rodriguez et al. (2004). Figure made with GeoMapApp (www.geomapapp.org) and Global Multi-Resolution Topography Data Synthesis (Ryan et al., 2009).

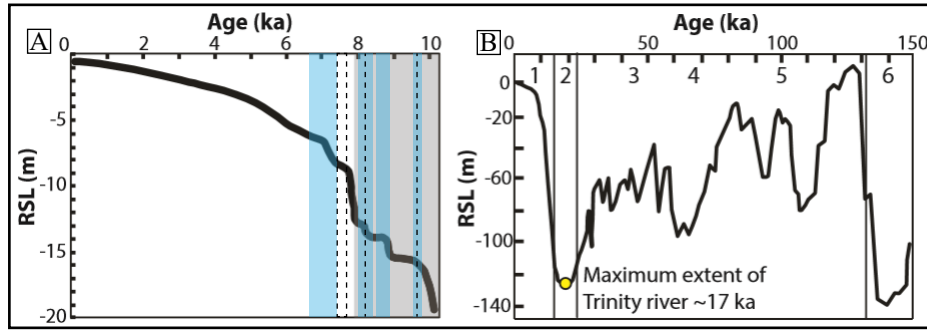


Figure 2. Holocene sea level curve. A) Sea level rise over the last 10 kyr with periods of rapid sea level rise identified by Milliken et al. (2008) (boxed in blue) and rapid sea level rise in Galveston Bay, Texas, identified by Anderson et al. (2008) (dashed lines). B) Holocene sea level curve over last 150 kyr showing Marine Isotope Stages 1-6 and maximum lowstand for the Trinity River occurring approximately 17 ka (modified from Swartz, 2019).

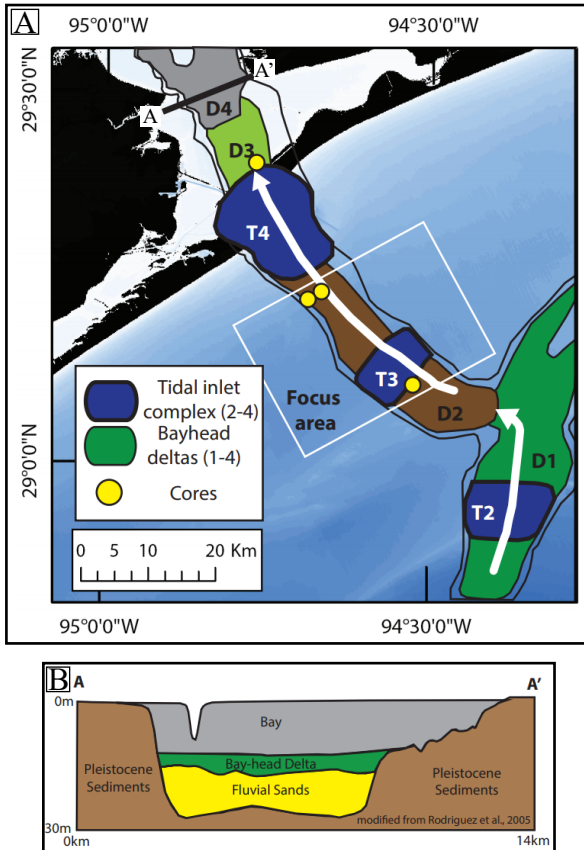


Figure 3. Trinity River transgressive systems tract. A) Landward changes of depositional facies due to Holocene sea level rise and study area offshore Galveston Bay, Texas. B) Cross-section of Trinity River Paleovalley within modern Galveston Bay, with generalized valley fill transitioning from fluvial sands to bay-head delta and bay fill deposits (modified from Swartz, 2019).

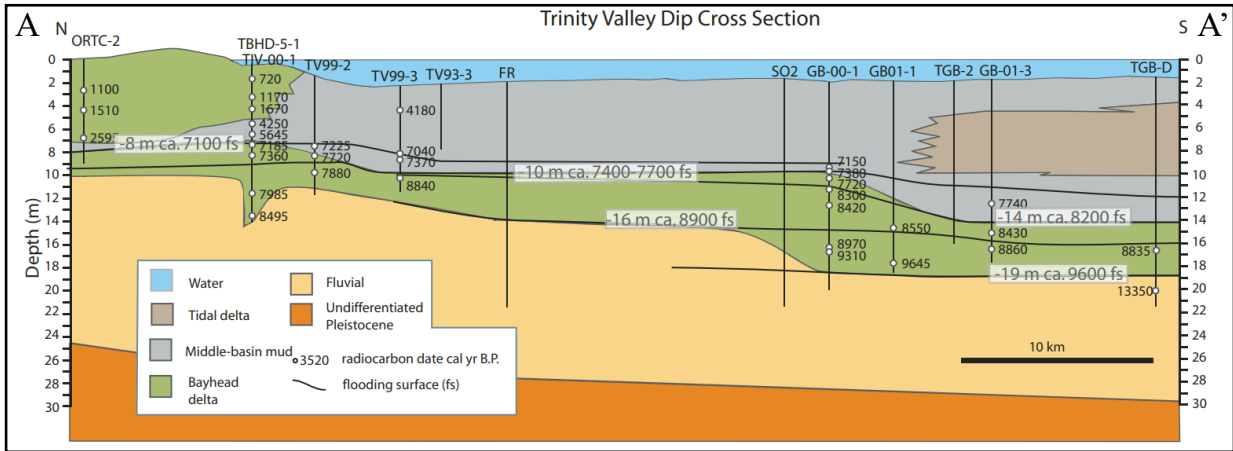


Figure 4. Cross section of the Trinity River Paleovalley in modern Galveston Bay, Texas (location in Figure 1), compiled from seismic and core data analyzed by Anderson Group displaying prominent sedimentary facies and flooding surfaces with radiocarbon ages (modified from Anderson et al., 2008).

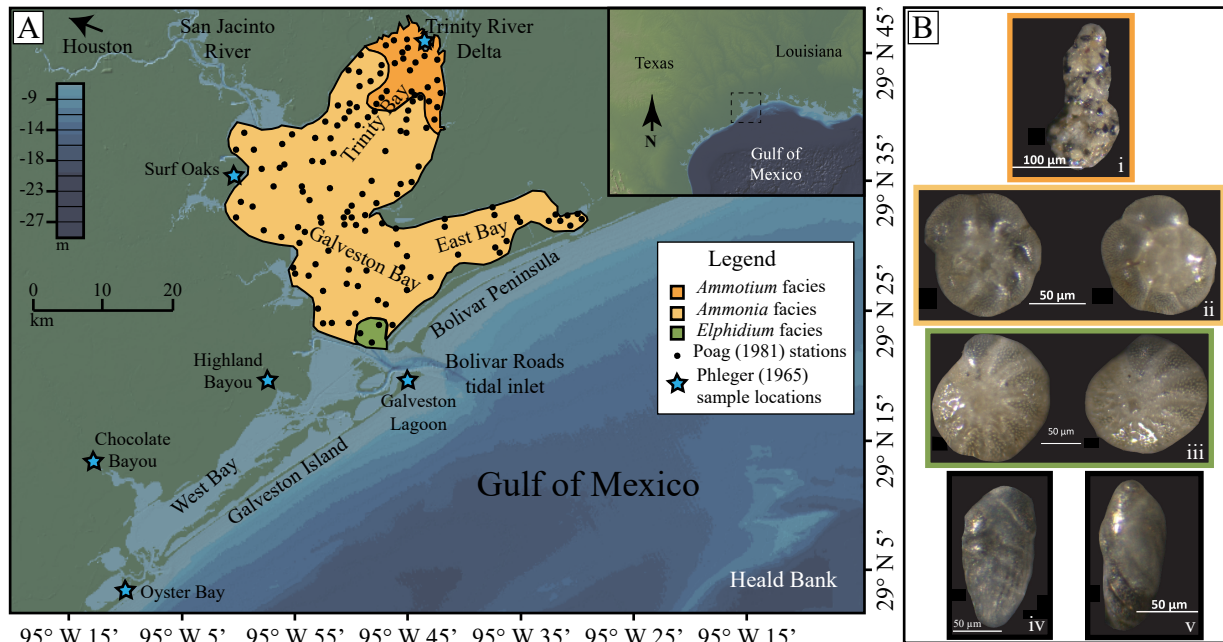


Figure 5. Foraminiferal predominance facies of Galveston Bay, Texas, based on Poag (1981). A) Map of Galveston Bay, Texas, showing areas within the modern estuary that are dominated by specific genera of foraminifera, and locations of marshes (blue stars) studied by Phleger (1965). B) Images of dominant genera of foraminifera: i) *Ammotium salsum* (orange; upper bay facies), ii) *Ammonia* sp. (yellow-orange; central bay facies), iii) *Elphidium* sp. (green; outer bay facies), iv and v) *Bolivina* sp. and *Bulimina* sp., respectively, which are diagnostic genera for inner shelf facies (Culver, 1988) (modified from Poag, 1981, and Phleger, 1965). Figure made with GeoMapApp (www.geomapapp.org) and Global Multi-Resolution Topography Data Synthesis (Ryan et al., 2009).

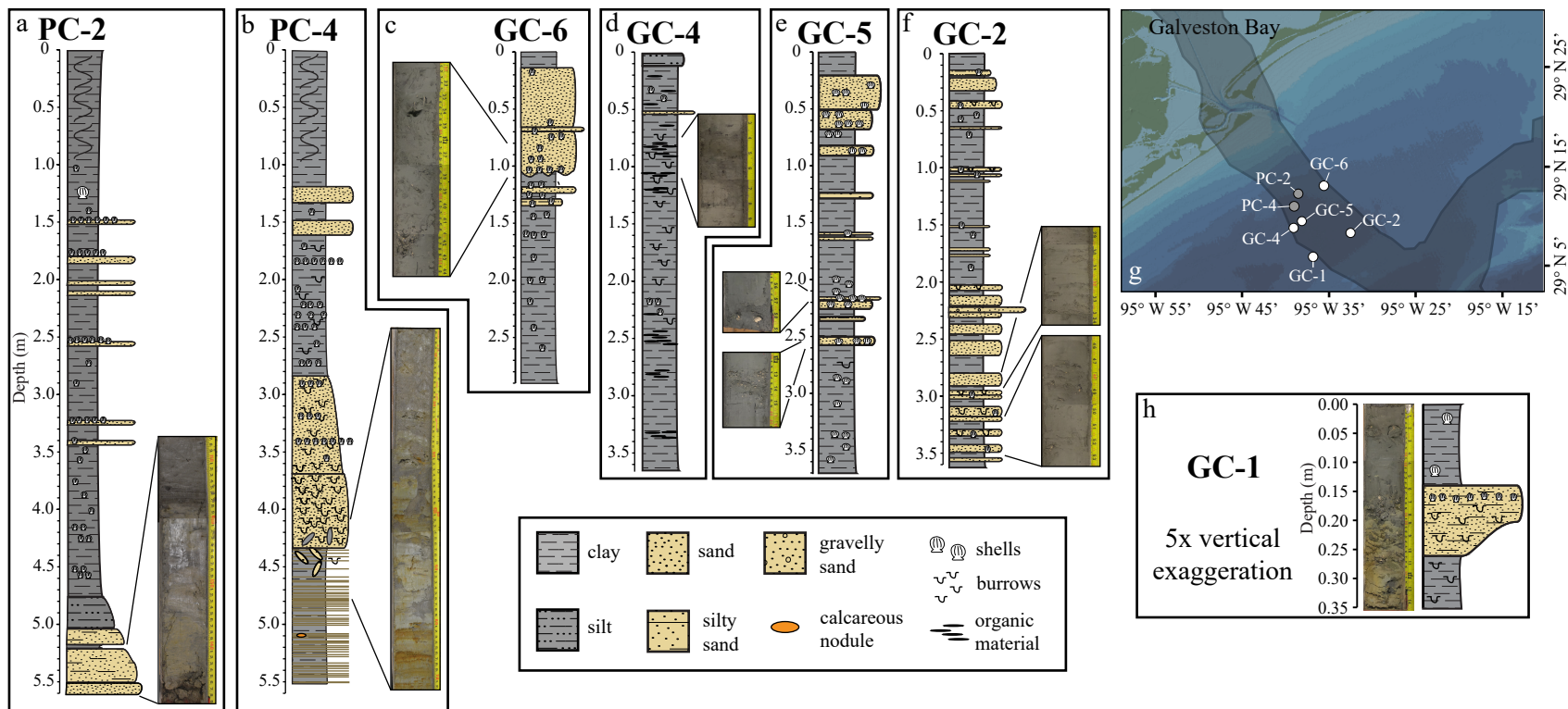


Figure 6. Stratigraphic columns and select core images from this study. a) PC-2 column with image of fluvial and upper bay sands (~5.2-5.6 m); b) PC-4 column with image of the Pleistocene terrace with oxidized sand in clay to upper bay heavily burrowed sands (~4.1-4.8 m); c) GC-6 column with image of outer bay shelly sands (0.8-1.1 m); d) GC-4 column with image of organic material (0.7-1.1 m); e) GC-5 column with images of large shells (2.1-2.2 m) and shell hash (2.5-2.6 m) in sandy sections; f) GC-2 column with images of sandy intervals containing shell fragments (2.8-2.9 m and 3.2-3.5 m); g) map of core locations offshore Galveston Bay; and h) GC-1 column and image of entire core (not at same scale as other cores).

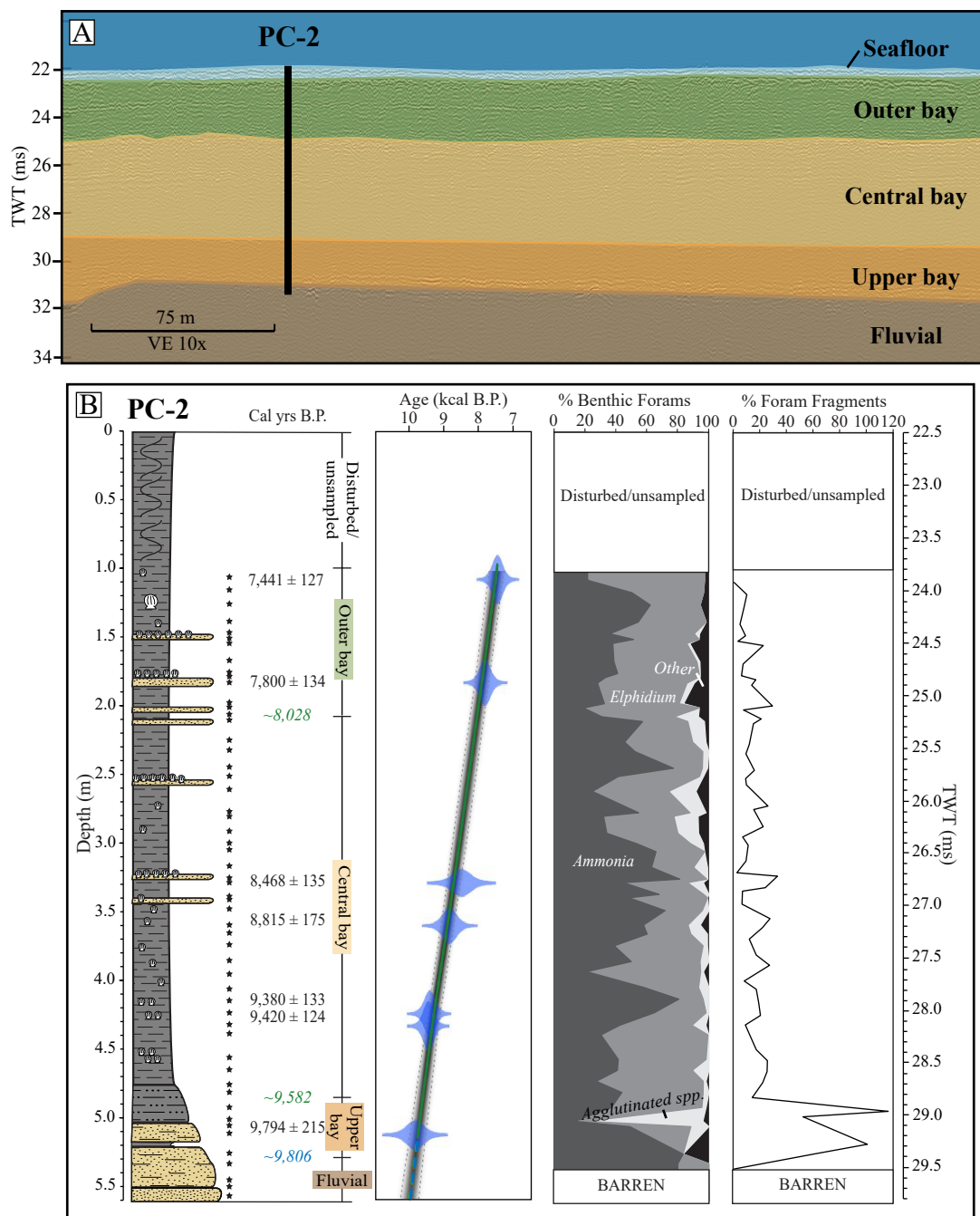


Figure 7. Piston Core 2 (PC-2). A) Interpreted seismic data with approximate depth of penetration for PC-2 (location in Figure 6). Seismic interpretation from Burstein et al. (2021) (VE = vertical exaggeration). B) Stratigraphic column of PC-2 displaying sample locations (black stars), carbon dates (black), and interpolated (green) and extrapolated (blue ages from age model. Age model based off of radiocarbon ages (blue ovals tapering to error range), with mean age depicted by solid dark green line for interpolated ages, light green dashed line for extrapolated ages, and gray scale out to 95% confidence interval predicted by the model. Interpreted depositional facies based off of foraminiferal assemblage abundances and percent foram fragments. Two-way travel time scale for stratigraphic column in ms calculated from approximate seismic velocity of 1,525 m/s starting at time of seafloor.

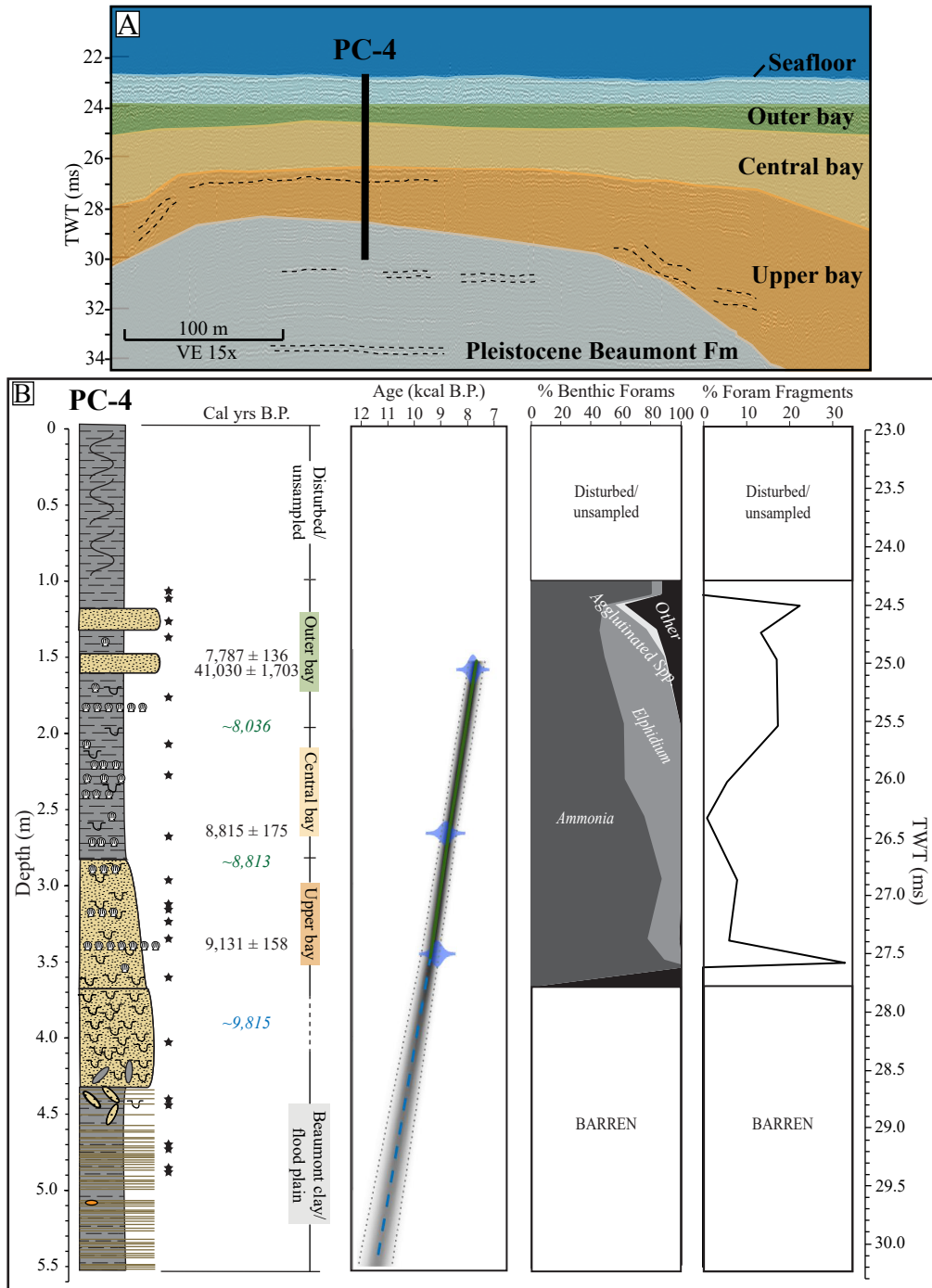


Figure 8. Piston Core 4 (PC-4). A) Interpreted seismic data with approximated depth for PC-4 into a Pleistocene terrace (location in Figure 6). Seismic interpretation from Burstein et al. (2021) (VE = vertical exaggeration). B) Stratigraphic column with sample locations (black stars), carbon dates (black text), and interpolated (green) and extrapolated (blue) ages from age model. Age model based off of radiocarbon ages (blue ovals tapering to error range), with mean age depicted by dark green solid line for interpolated ages, light green dashed line for extrapolated ages, and gray scale out to 95% confidence interval predicted by the model. Interpreted depositional facies based off of foraminiferal assemblage abundances and percent foram fragments. Two-way travel time scale for stratigraphic column in ms calculated from approximate seismic velocity of 1,525 m/s starting at time of seafloor.

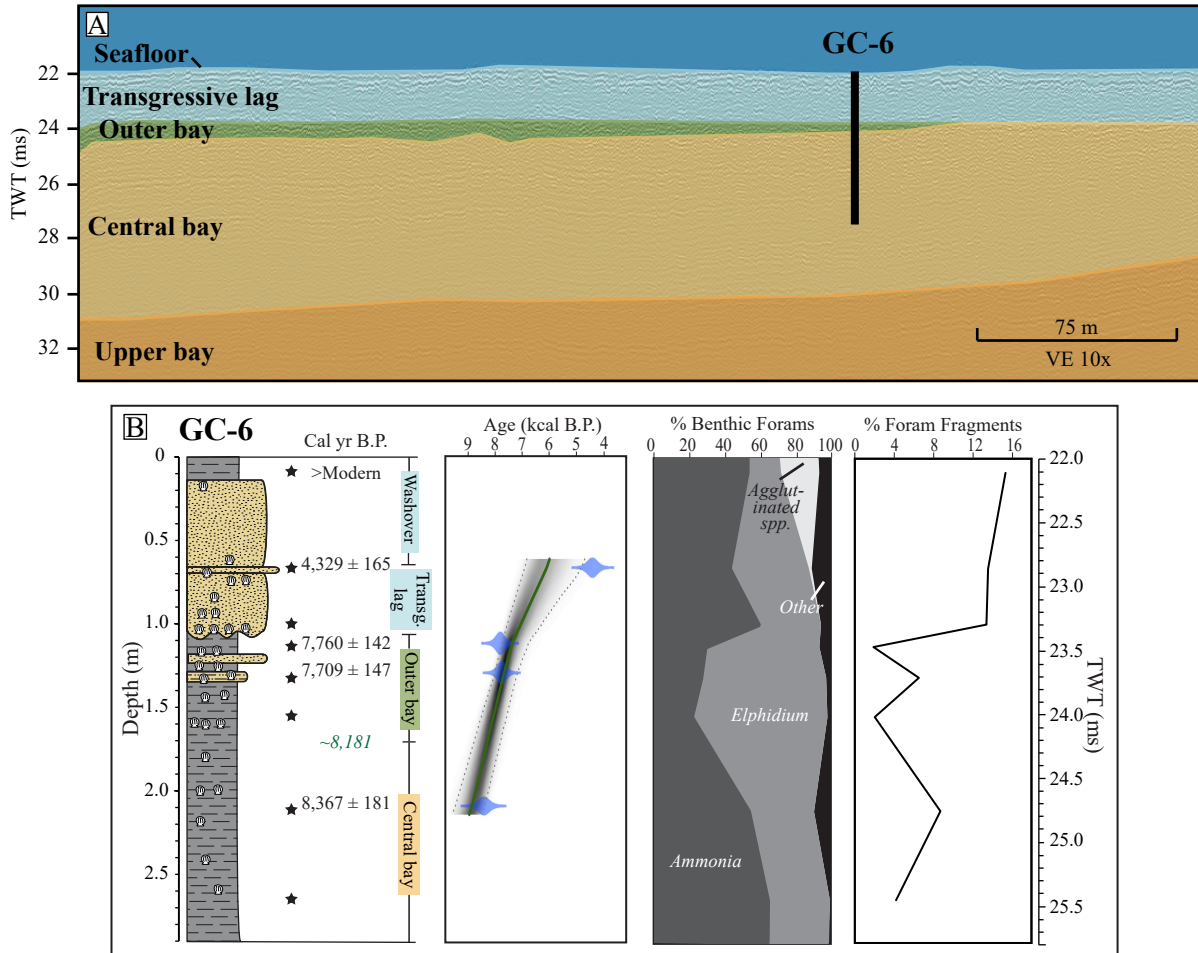


Figure 9. Gravity Core 6 (GC-6). A) Interpreted seismic data with approximate depth of penetration for GC-6 (location in Figure 6). Seismic interpretation from Burstein et al. (2021) (VE = vertical exaggeration). B) Stratigraphic column with sample locations (black stars), radiocarbon dates (black text), interpolated ages (italicized in green) based off of age model. Age model based off of radiocarbon ages (blue ovals tapering to error range), with mean age depicted by solid green line and gray scale out to 95% confidence interval predicted by the model. Interpreted depositional facies based off of foraminiferal assemblage abundances and percent foram fragments. Two-way travel time scale for stratigraphic column in ms calculated from approximate seismic velocity of 1,525 m/s starting at time of seafloor.

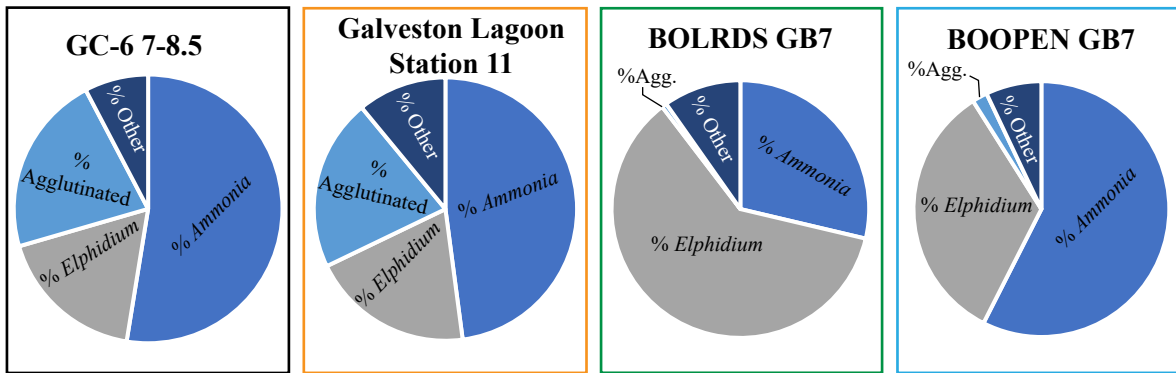
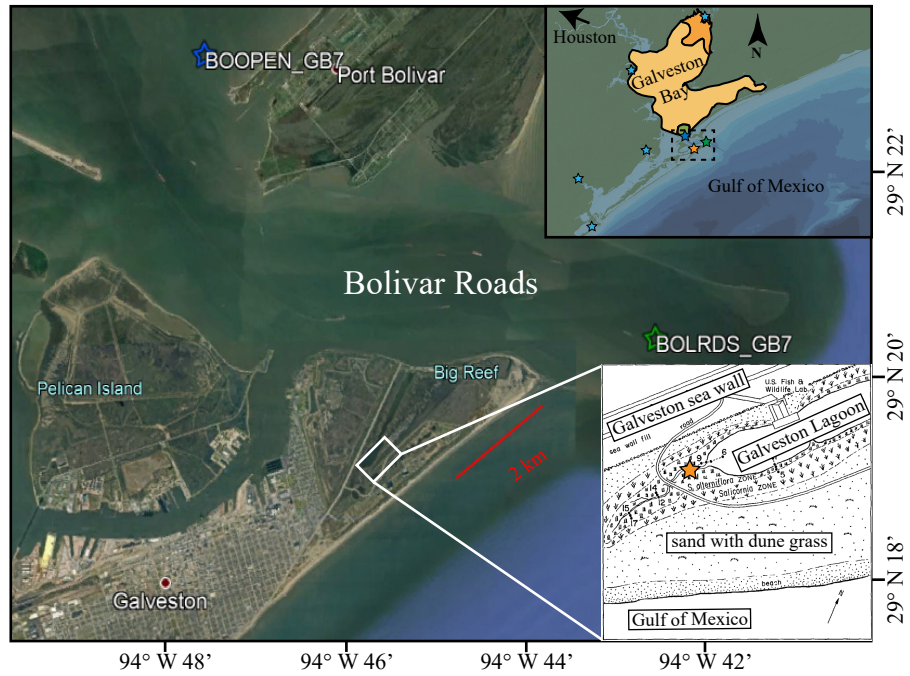


Figure 10. Comparison of GC-6 upper sample (7-8.5 cm) to modern foram assemblages: Galveston Lagoon sample from Station 11 analyzed by Phleger (1965) (orange), BOLRDS GB7 grab sample taken from the outer edge of the tidal inlet (green), and BOOPEN GB7 grab sample taken from the inner edge of the tidal inlet (blue). The Station 11 sample is the closest approximation to the GC-6 sample. Image source Google Earth (2021).

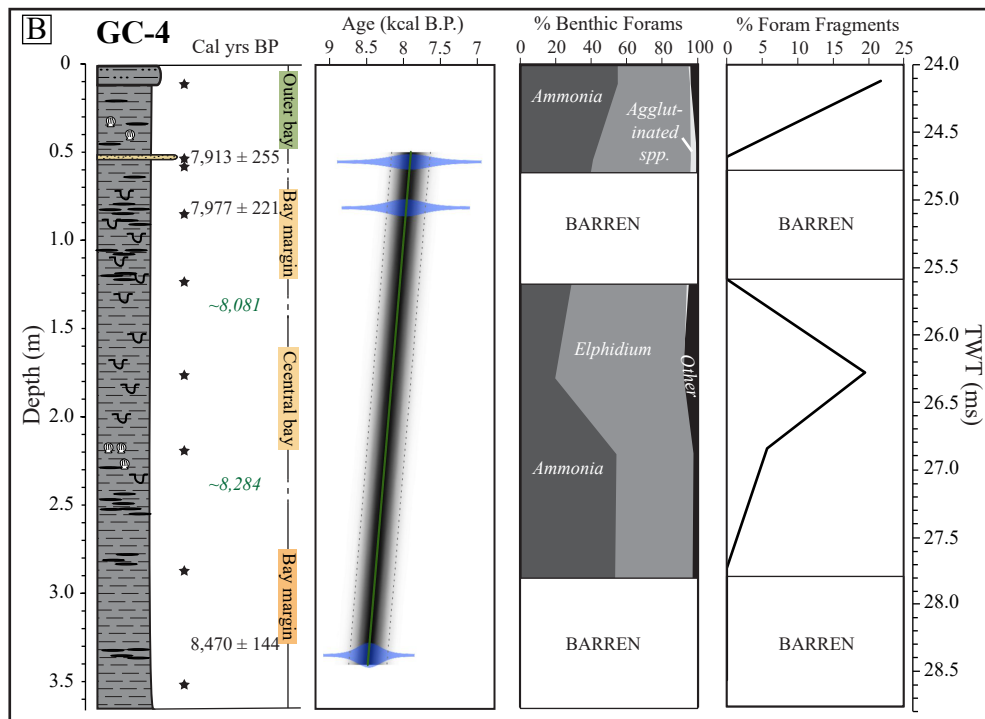
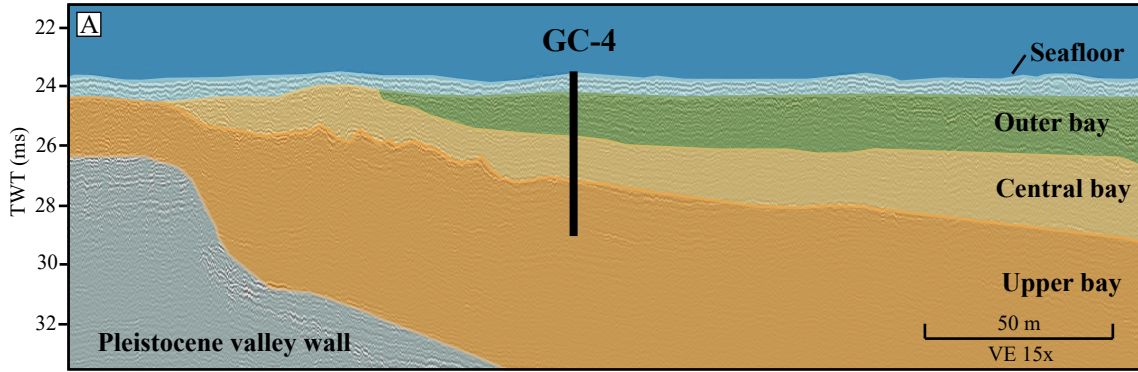


Figure 11. Gravity Core 4. A) Interpreted seismic data with approximate depth of penetration for GC-4 (location in Figure 6). Seismic interpretation from Burstein et al. (2021) (VE = vertical exaggeration). B) Stratigraphic column of GC-4 showing samples (black stars) with radiocarbon ages (black text), interpolated ages (italicized in green) from age model. Age model based off of radiocarbon ages (blue ovals tapering to error range), with mean age depicted by solid green line and gray scale out to 95% confidence interval predicted by the model. Interpreted depositional facies based off of foraminiferal assemblage abundances and percent foram fragments. Two-way travel time scale for stratigraphic column in ms calculated from approximate seismic velocity of 1,525 m/s starting at time of seafloor.

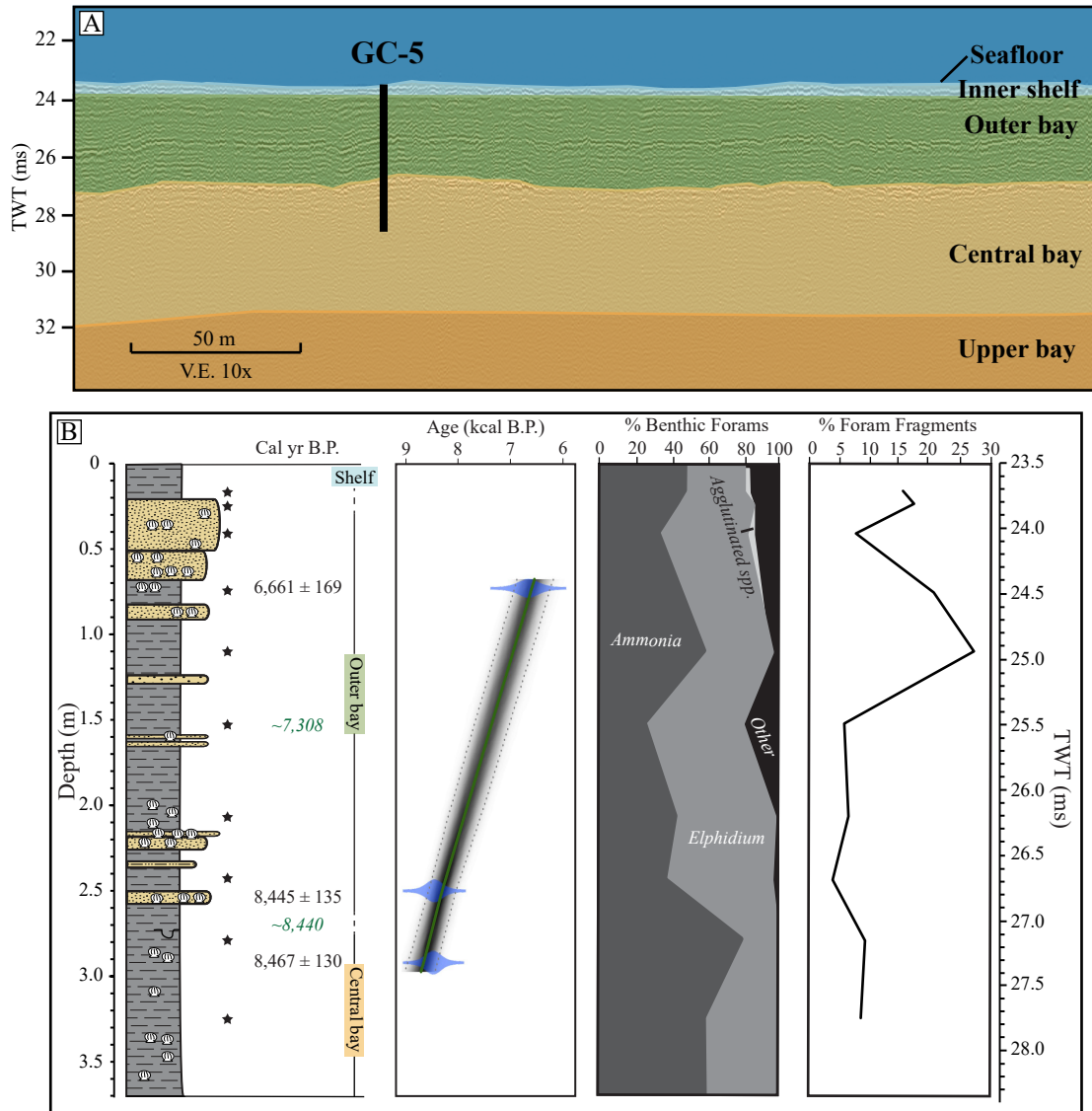


Figure 12. Gravity Core 5. A) Interpreted seismic data with approximate depth of penetration for GC-5 (location in Figure 6). Seismic interpretation from Burstein et al. (2021) (VE = vertical exaggeration). B) Stratigraphic column of GC-5 showing samples (black stars) with radiocarbon ages (black text), interpolated ages (italicized in green) from age model. Age model based off of radiocarbon ages (blue ovals tapering to error range), with mean age depicted by solid green line and gray scale out to 95% confidence interval predicted by the model. Interpreted depositional facies based off of foraminiferal assemblage abundances and percent foram fragments. Two-way travel time scale for stratigraphic column in ms calculated from approximate seismic velocity of 1,525 m/s starting at time of seafloor.

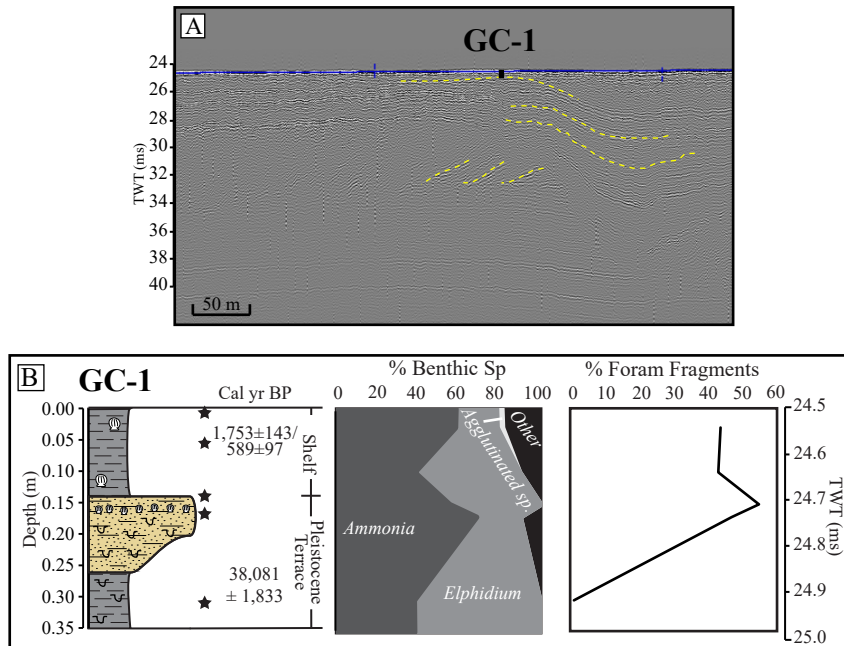


Figure 13. Gravity core 1 (GC-1). A) Uninterpreted seismic line showing location of GC-1 short core where it penetrated a high-elevation Pleistocene terrace. Yellow dashed lines show approximated interpretation of draped sediments and dipping reflectors. B) Stratigraphic column of GC-1 showing sample locations (black stars), radiocarbon dates, and interpreted depositional environments based on lithology, and foraminiferal assemblages and fragmentation. Two-way travel time (TWT) scale calculated based on approximate seismic velocity of 1,525 m/s starting at time of seafloor.

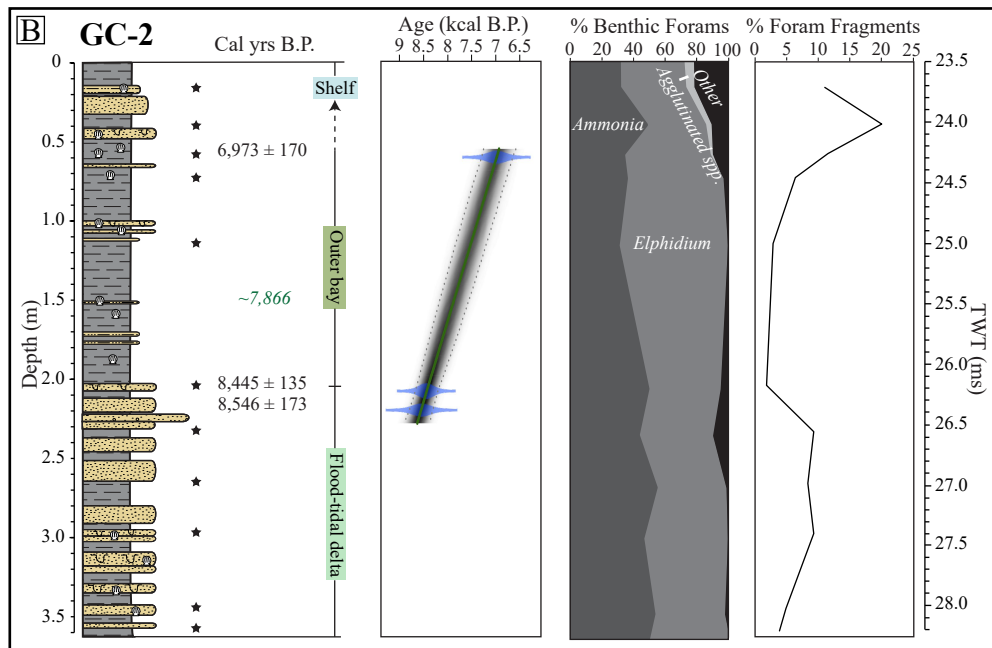
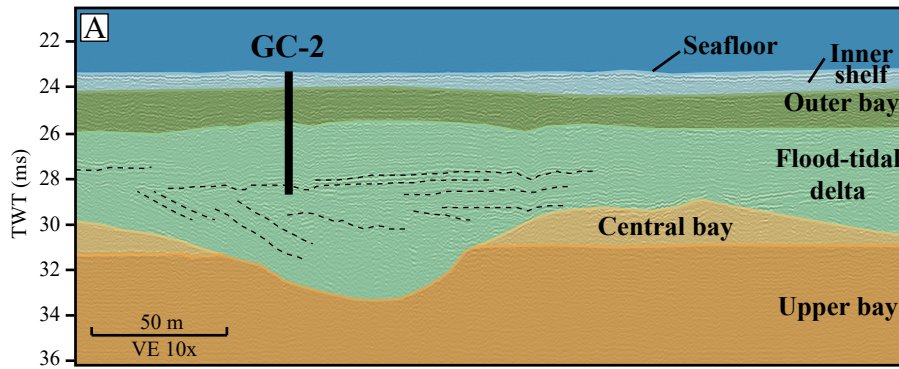


Figure 14. Gravity core 2 (GC-2). A) Interpreted seismic data with approximate depth of penetration for GC-2 (location in Figure 6). Seismic interpretation from Burstein et al. (2021) (VE = vertical exaggeration). B) Stratigraphic column with sample locations (black stars), radiocarbon dates (black text), interpolated ages (italicized in green) from age model. Age model based off of radiocarbon ages (blue ovals tapering to error range), with mean age depicted by solid green line and gray scale out to 95% confidence interval predicted by the model. Interpreted depositional facies based off of foraminiferal assemblages and percent foram fragments. Two-way travel time scale for stratigraphic column in ms calculated from approximate seismic velocity of 1,525 m/s starting at time of seafloor.

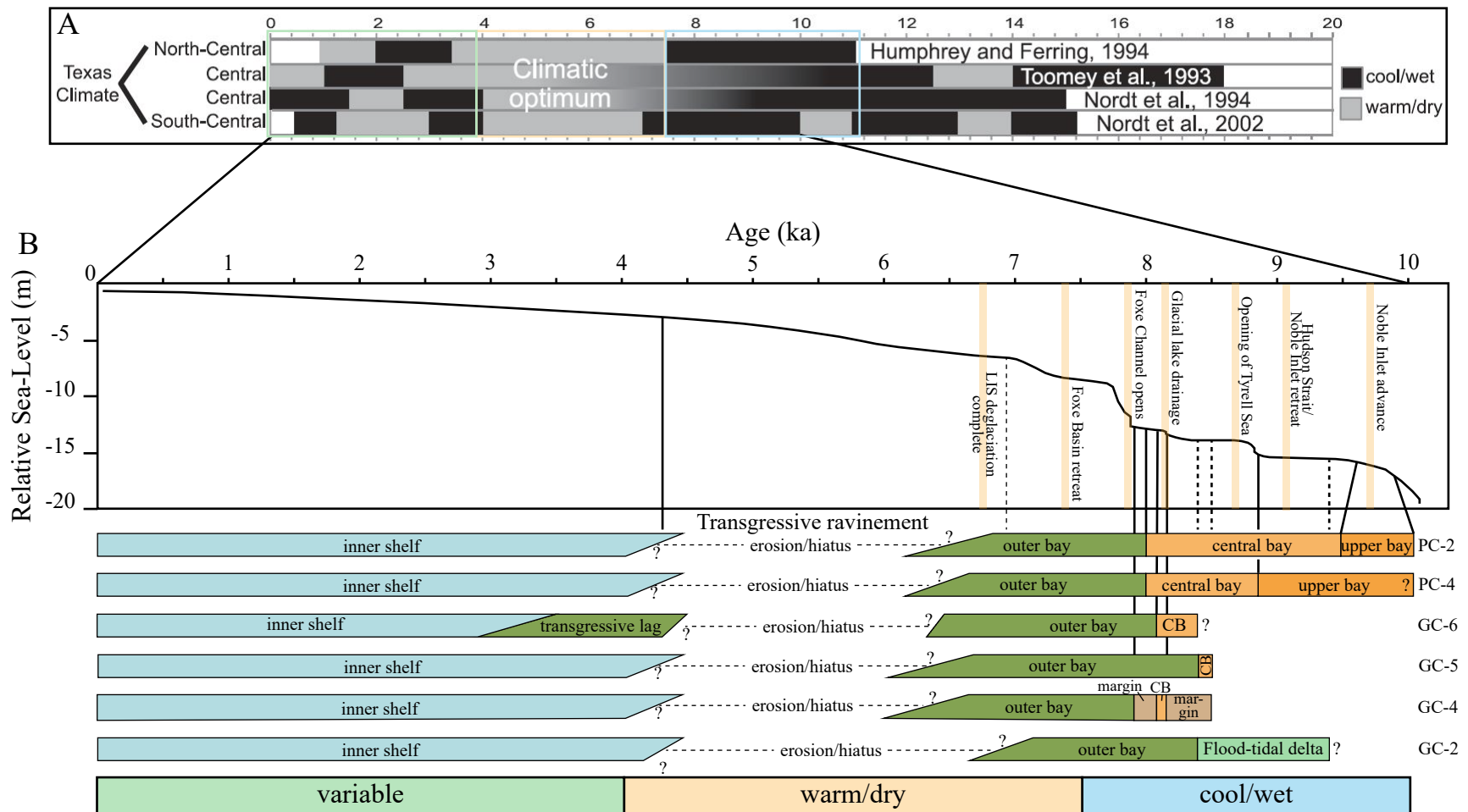


Figure 16. Timeline of environmental change and sea-level rise in Galveston paleostuary. A) Compilation of Gulf Coast climate for the Holocene (modified from Weight et al., 2011). B) Gulf Coast Holocene sea level curve containing prominent North American glacial events (beige lines) identified in Jennings et al. (2015) (modified from Swartz, 2019) and a compilation of environmental change within Trinity River paleovalley cores and approximated period of transgressive erosion. A majority of environmental transitions take place during a cool/wet climate when sea-level rise was more rapid, while significant transgressive erosion took place during a warm/dry period when sea-level rise slowed significantly.

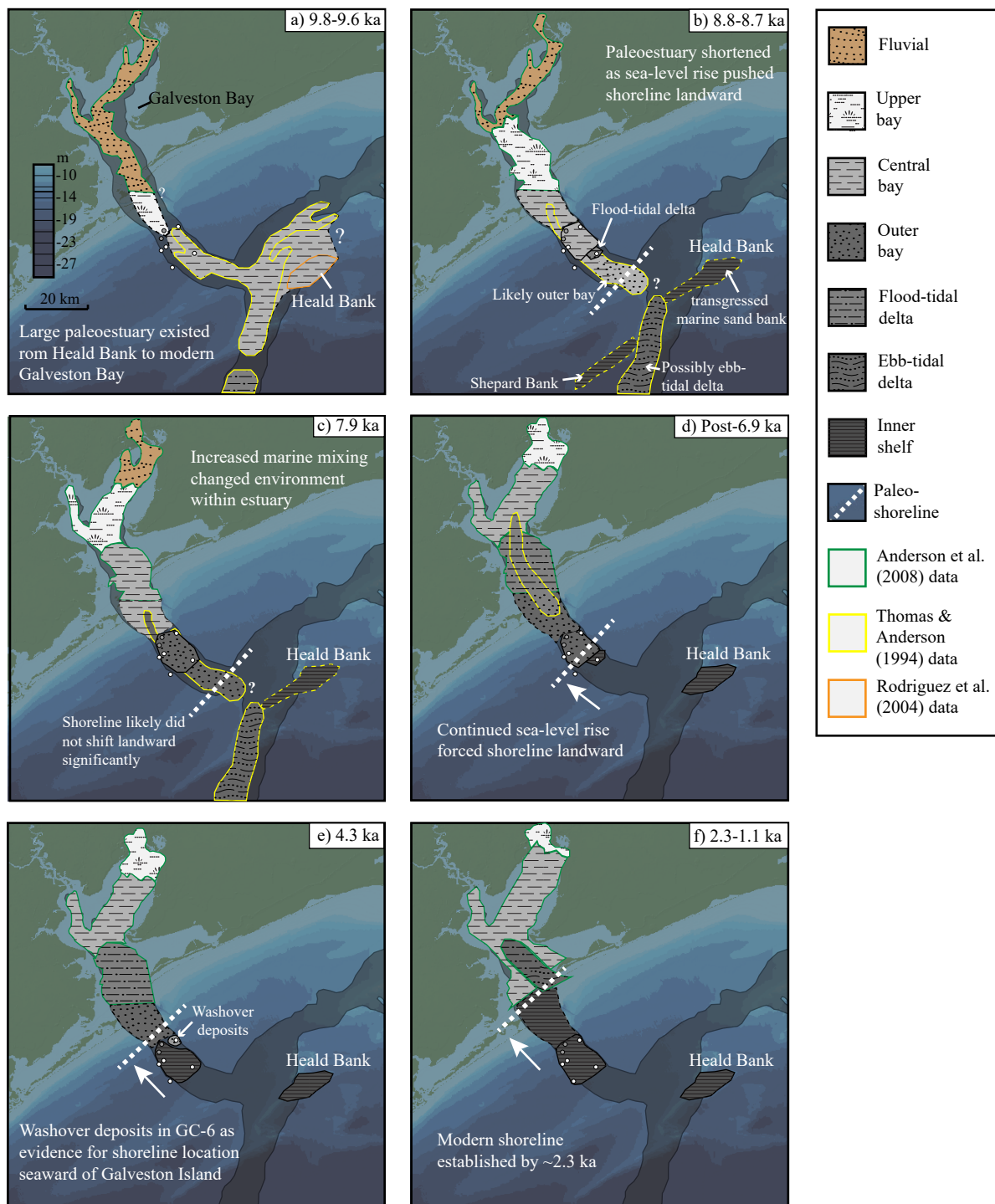


Figure 17. Summary of paleoenvironmental change of Holocene estuary offshore Galveston Bay, Texas. Environmental facies at specific periods of time are based on micropaleontological analysis of cores in study areas and combined with previous research (outlined in green, yellow, and orange), and inferences were made between these study areas (dashed outlines). Facies are mapped within the bounds of the incised valley, but likely extended beyond those boundaries; however, the outer boundaries are difficult to determine due to probable removal of sediments during marine transgression. Paleoshorelines are estimated based on proximity to tidal delta and outer bay environments, and identification of washover sediments in cores.